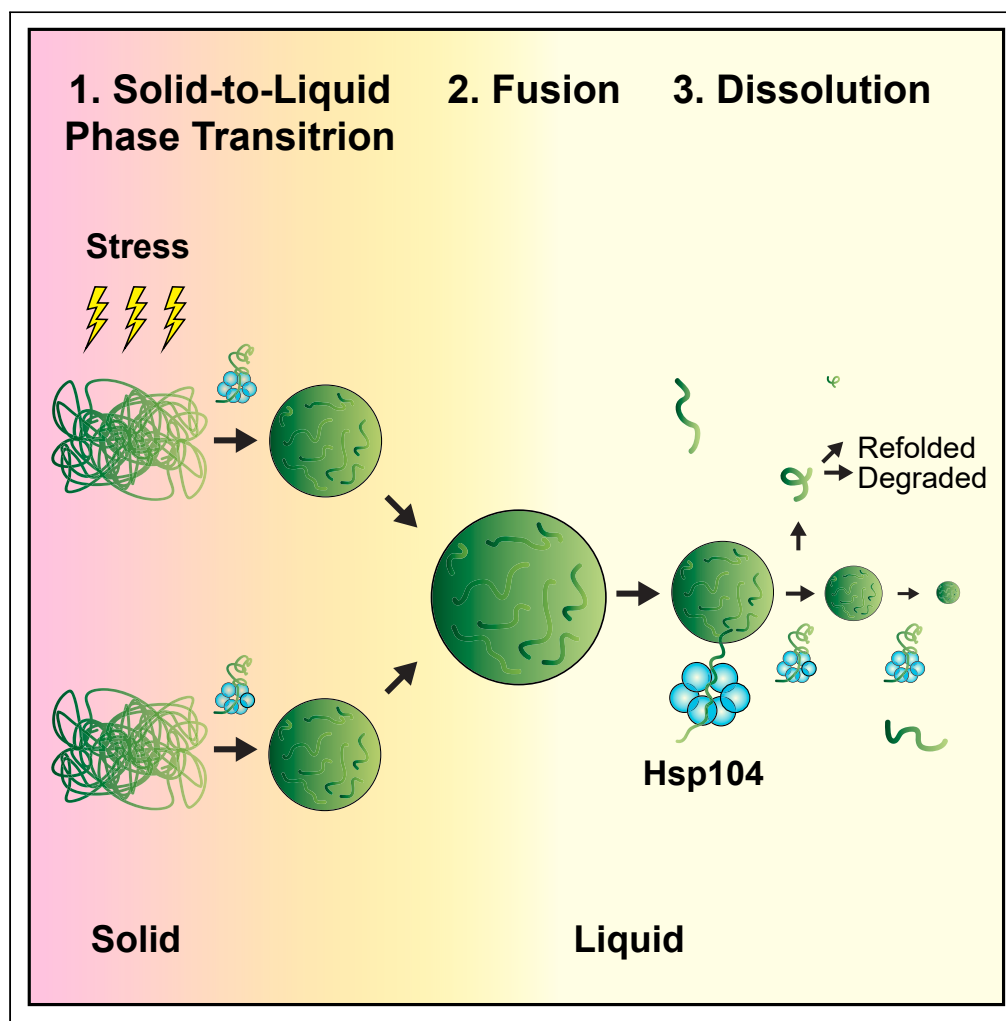


Article

Solid-to-liquid phase transition in the dissolution of cytosolic misfolded-protein aggregates



Alexis Tomaszewski, Rebecca Wang, Eduardo Sandoval, Jin Zhu, Jian Liu, Rong Li

rong@jhu.edu

Highlights

Aggregates undergo a solid-to-liquid phase transition after stress attenuation

Dissolution involves clustering followed by fusion reducing in both size and number

Hsp104 is required for both SLPT and subsequent dispersal of the liquid condensates

Reveal an unexpected mechanism of cellular control over protein disaggregation

Tomaszewski et al., iScience 26, 108334
December 15, 2023 © 2023 The Author(s).
<https://doi.org/10.1016/j.isci.2023.108334>

Article

Solid-to-liquid phase transition in the dissolution of cytosolic misfolded-protein aggregates

Alexis Tomaszewski,^{1,2} Rebecca Wang,³ Eduardo Sandoval,⁴ Jin Zhu,⁵ Jian Liu,^{1,2} and Rong Li^{1,2,5,6,7,*}

SUMMARY

Accumulation of protein aggregates is a hallmark of cellular aging and degenerative disorders. This could result from either increased protein misfolding and aggregation or impaired dissolution of aggregates formed under stress, the latter of which is poorly understood. In this study, we employed quantitative live-cell imaging to investigate the dynamic process of protein disaggregation in yeast. We show that protein aggregates formed upon heat stress are solid condensates, but after stress attenuation these protein aggregates first transition into a liquid-like state during their dissolution. This solid-to-liquid phase transition (SLPT) accompanies the reduction in aggregate number due to the fusion of the liquid condensates. The chaperone activity of Hsp104, a Clp/HSP100 family chaperone, is required for both SLPT and subsequent dispersal of the liquid condensates. Sse1, a yeast HSP110 chaperone, also facilitates SLPT. These results illuminate an unexpected mechanistic framework of cellular control over protein disaggregation upon stress attenuation.

INTRODUCTION

The clearance of misfolded proteins to maintain cellular proteostasis is a highly regulated process involving chaperones and protein turnover machineries.^{1–4} During the natural aging process, an unbalanced proteostasis can lead to the accumulation of misfolded proteins that aggregate together to form solid inclusions or amyloid plaques.^{5–8} Protein misfolding and aggregation have been implicated in numerous neurodegenerative diseases such as Alzheimer's disease, amyotrophic lateral sclerosis, Huntington's disease, and Parkinson's disease.^{1,3,9–11} Studies on protein aggregation have shown that the formation of solid protein aggregates, especially those involved in degenerative disease, occur through liquid-liquid phase separation followed by liquid-to-solid phase transition.^{12–16}

Protein aggregation, however, is not always associated with disease states and can occur in normal cells under proteotoxic stresses such as heat shock, oxidation, and proteasome inhibition.^{9,17} Increasing evidence suggests that healthy cells have the ability to clear stress-induced protein aggregates via the action of molecular chaperones.^{2,18–20} The best studied system is the budding yeast, where the chaperone protein Hsp104, a hexameric AAA+ ATPase, works with Hsp40 and Hsp70 chaperones to bind and disentangle aggregated or amyloid proteins by translocating them through a central channel.^{18,21–23} *In vitro*, the disaggregase activity of Hsp104 can be assayed via the reactivation of a denatured firefly luciferase.²¹ Using purified components in a minimal system, it was shown that Hsp104 requires both polypeptide substrate binding and ATP hydrolysis to reactivate the misfolded protein. This system has been adapted to identify variants that suppress the toxicity of disease-related proteins.^{24–27} Although mammalian cells do not possess Hsp104 orthologs, HSP70 in combination with HSP110 resolubilize aggregated proteins so that they can be refolded or degraded *in vitro*.^{28–33}

The accumulation of pathological aggregates could therefore result from either increased aggregate formation or impaired dissolution. A detailed understanding of how protein aggregates are resolved may illuminate approaches to more effectively clear toxic misfolded proteins or prevent them from accumulating as toxic aggregates during aging. Here, we characterized the process of protein dissolution after heat stress in budding yeast by quantitative live-cell imaging. We found surprisingly that protein disaggregation undergoes a solid-to-liquid phase transition (SLPT). Importantly, this transition and the subsequent dissolution of the liquid intermediate both require the chaperone activity of Hsp104.

RESULTS

Protein aggregates undergo solid-to-liquid phase transition during dissolution process

To investigate how aggregates of misfolded proteins are dissolved, we stressed budding yeast cells expressing a green fluorescent protein (GFP)-tagged thermolabile protein, firefly luciferase R188Q single mutant (FlucSM-GFP),³⁴ with a 30 min heat shock (HS) at 42°C, during which

¹Center for Cell Dynamics and Department of Cell Biology, Johns Hopkins University School of Medicine, Baltimore, MD 21205, USA

²Biochemistry, Cellular and Molecular Biology (BCMB) Graduate Program, Johns Hopkins University School of Medicine, Baltimore, MD 21287, USA

³Hackensack Meridian School of Medicine, Nutley, NJ 07110, USA

⁴Department of Neuroscience, University of California, Berkeley, Berkeley, CA 94720, USA

⁵Mechanobiology Institute, National University of Singapore, Singapore 117411, Singapore

⁶Department of Biological Science, National University of Singapore, Singapore 117411, Singapore

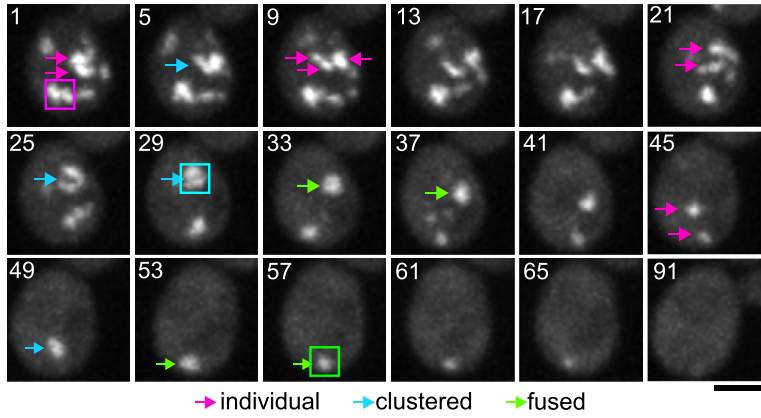
⁷Lead contact

*Correspondence: rong@jhu.edu

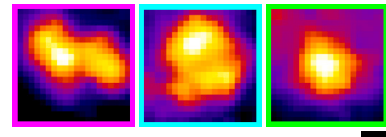
<https://doi.org/10.1016/j.isci.2023.108334>



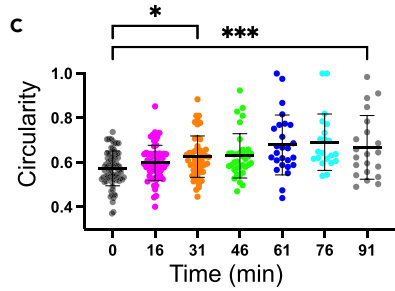
A FlucSM-GFP WT



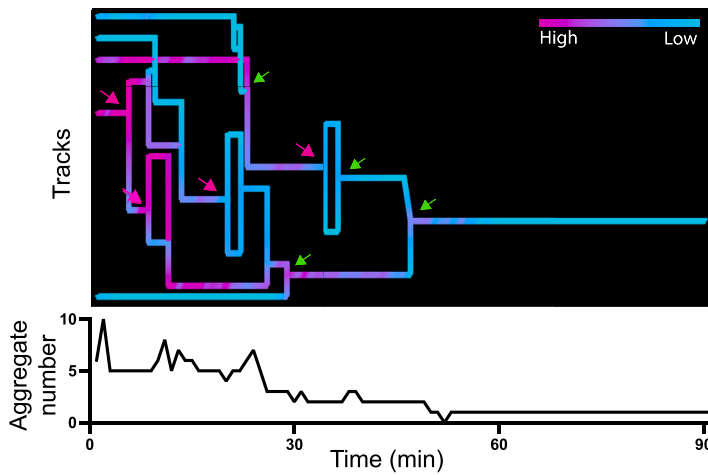
B



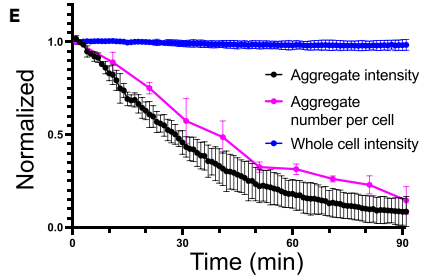
C



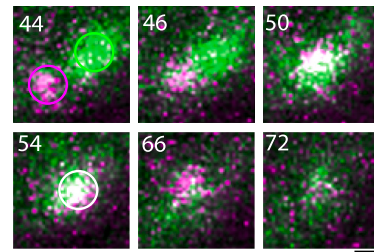
D



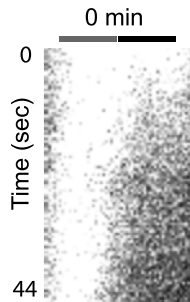
E



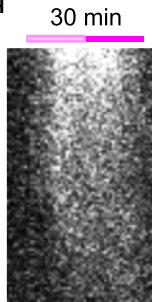
F FlucSM-mEos3.2 WT



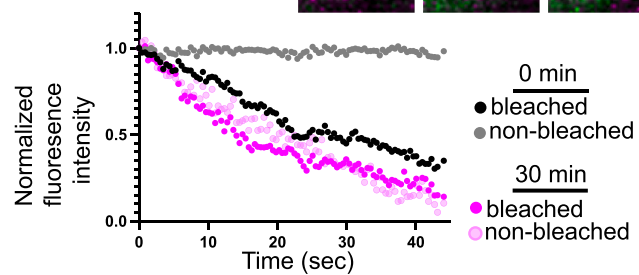
G



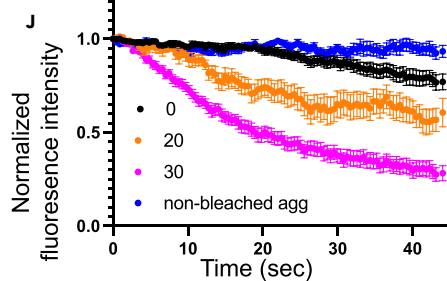
H



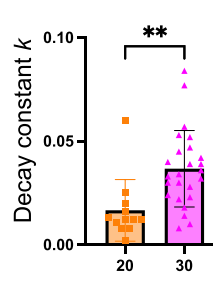
I



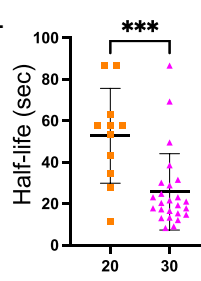
J



K



L



M

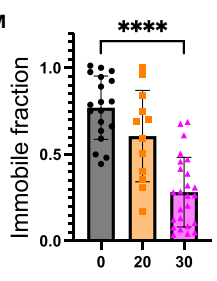


Figure 1. Protein aggregates undergo a solid to liquid-like phase transition during the dissolution process

- (A) Time-lapse confocal imaging of a single yeast cell expressing FlucSM-GFP labeled aggregates after a 30 min heat shock (HS) at 42°C and shifted back to their permissive temperature of 30°C for 90 min. Scale bar, 2 μm.
- (B) Zoom in of individual rugged aggregates (pink box), aggregates that are beginning to come together and cluster (blue box), and aggregates once they have fused together (green box) displayed with fire LUTs. Scale bar, 0.5 μm.
- (C) Quantification of aggregate circularity after HS during dissolution. Each dot represents the circularity of a single aggregate. N = 3 movies. Error bars represent the SD. Statistical analysis was performed via a one-way ANOVA with a p value < 0.05 followed by a Tukey post hoc test with the following significance cut-off: not significant (ns): p > 0.05, *: p ≤ 0.05, **: p ≤ 0.01, ***: p ≤ 0.001, ****: p ≤ 0.0001.
- (D) Lineage trace of FlucSM-GFP labeled aggregates (top) and aggregate number (bottom) over time from the representative time-lapse movie of the cell from (A). Aggregates were detected and tracked in Imaris so that each line represents a track from an individual spot at each time point. Pink arrows represent events where a clustered aggregate moves apart and green arrows represent fusion events. The color represents the mean intensity of the aggregate in the track; pink denotes high intensity and blue denotes low intensity aggregates.
- (E) Normalized mean aggregate intensity, whole cell intensity, and aggregate number per cell of FlucSM-GFP labeled aggregates following HS. Time represents the number of minutes after shifting back to permissive temperature of 30°C (n = 3 movies and 96 cells). Error bars represent the SD.
- (F) Representative images from FlucSM-mEOS3.2 photoconversion experiment. Photoconverted aggregate after HS is circled with a pink circle and the non-converted aggregate is circled in green. Over time, these aggregates come together and the fused aggregate is circled in white. Time is represented in minutes. Scale bar, 0.5 μm.
- (G and H) Representative kymograph through the bleached half and non-bleached aggregate half of a FlucSM-GFP labeled aggregate at 0 min (G) and 30 min (H) after HS. For 0 min after HS: the bleached region (black line) and non-bleached region (gray line). For 30 min after HS: the bleached region (pink line) and non-bleached region (light pink line). Scale bar, 0.5 μm.
- (I) Quantification of the fluorescence intensity decay of the bleached half and non-bleached half of FlucSM-GFP aggregates at 0 and 30 min after HS depicted in G and H.
- (J) Normalized mean aggregate intensity and SEM for FLIP experiments acquired 0, 20, and 30 min after HS (n = 20, n = 12, and n = 25 respectively). Also included is the control normalized fluorescence intensity of a non-bleached aggregate in the same field as bleached aggregates at 0 min time point (n = 14 aggregates). Decay rate k (K), half-life (L), and immobile fraction (M) from the non-bleached half of the aggregate whose other half was being photobleached. Individual data points represent a single bleached aggregate. Statistical analysis was performed via an unpaired two-tailed t-test with the following significance cut-off: not significant (NS): p > 0.05, *: p ≤ 0.05, **: p ≤ 0.01, ***: p ≤ 0.001, ****: p ≤ 0.0001.

aggregates labeled with FlucSM-GFP was observed to form. After the cells were shifted back to the permissive temperature of 30°C, protein aggregates dissolve in approximately 90 min (Figure 1A and Video S1). Immediately after HS, cells contained many FlucSM-GFP aggregates that generally have a jagged shape, characteristic of solid structures (Figure 1B, left panel) and transform into rounder structures during the dissolution process (Figure 1B, right panel). Quantification of circularity shows that over time aggregates became significantly more circular after 30 min and continued to increase in circularity prior to dissolving (Figure 1C).

We used lineage tracing to follow the fate of individual aggregates during dissolution (Figure 1D, an example). Within the first 30 min of recovery, mobile aggregates came in close proximity to other aggregates but did not often stay together. We refer this behavior as “clustering.” After a 30 min recovery, aggregates tended to fuse together after clustering (Figure 1B). We consider these events “fusion,” which was also reported in previous studies.^{35,36} Both the intensity of the aggregates and number decreased over the 90 min period as aggregates fused and dissolved (Figures 1D and 1E). Quantification of whole cell intensity shows that during dissolution FlucSM-GFP levels remained mostly constant (Figure 1E), and so the loss of aggregate intensity was not due to the depletion of the protein in the cytoplasm. This was further confirmed with immunoblot analysis (Figures S1F and S1G).

To better differentiate aggregate clustering from fusion, we labeled aggregates with the photoconvertible fluorescent protein mEos3.2 and photoconverted single aggregates from green to pink 0 min after HS and tracked their fate during dissolution.³⁷ If a pink, photoconverted aggregate fuses with a green, non-photoconverted aggregate, the fused aggregate would appear white, but if these aggregates only cluster without fusion the different fluorescent color would occupy different spatial domains of an aggregate (Figure S1A). Figure 1F shows an example of first clustering and then fusion, where the photoconverted pink aggregate came in close proximity to a non-converted green aggregate and initially occupied separate domains. After ~10 min, these two aggregates fused and stayed together (Figure 1F and also Figure S1D). We quantified the normalized fluorescence intensity of the converted and original aggregates relative to the converted aggregate. When the photoconverted aggregate fuses with the original aggregate, there was a spike in total intensity, consistent with the two aggregates occupying the same domain, which was followed by simultaneous decrease in the fluorescence intensity of both species during dissolution (Figure S1E).

The ability to fuse and the transition into more rounded structures suggested that the aggregates might undergo SLPT. To test this, we performed fluorescence loss in photobleaching (FLIP) assay, wherein half of a protein aggregate was continuously photobleached for 44 s either immediately after HS (0 min), or 30 min after shifting to back 30°C after HS (30 min). Fluorescence decay of the non-photobleached half would reflect the diffusion of non-bleached molecules into the area being bleached. Rapid molecular diffusion is expected within liquid-like but not solid-like condensates.¹² Little diffusion was observed in the aggregates 0 min after HS (Figures 1G–1I). This is characteristic of solid structures and consistent electron microscopy images of protein aggregates immediately after HS which showed that aggregates are amorphous structures with compacted globular densities.^{38,39} However, the protein aggregates after a 30 min recovery showed fast molecular diffusion within, as the fluorescence in the non-bleached half decayed within seconds (Figures 1G–1L). Quantification of immobile fractions between the two time points showed that the mean immobile fraction progressively reduced with increasing time of recovery (Figure 1M). To control for off-target photobleaching in the FLIP experiments, fluorescence changes were quantified for a non-bleached aggregate in the

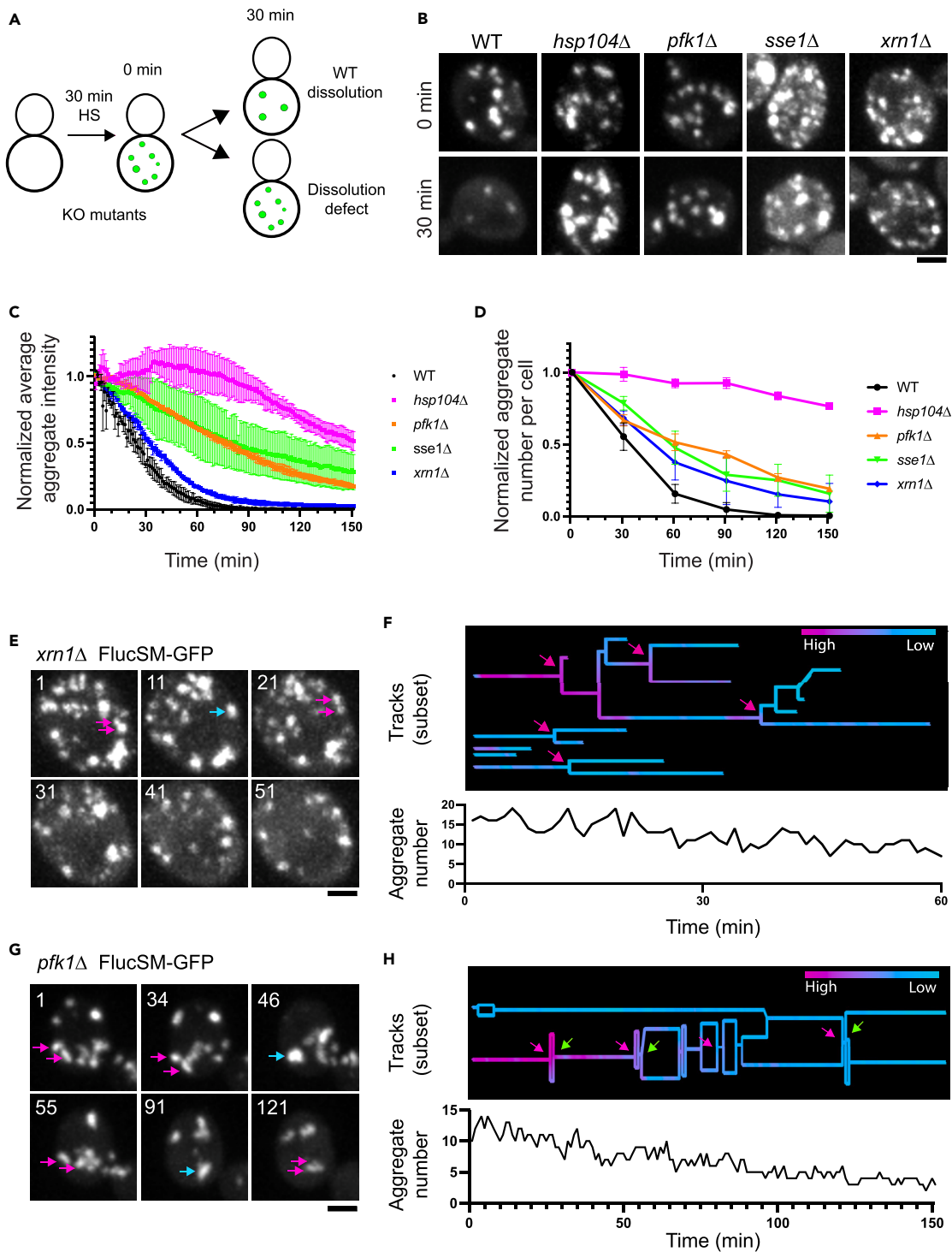


Figure 2. Molecular determinants of aggregate dissolution

(A) Screen schematic to identify proteins involved in aggregate dissolution. Aggregate enriched proteins were knocked out, labeled with FlucSM-GFP, subjected to a 30 min HS and imaged at 0 and 30 min after HS. Aggregate number was quantified (as in Figure S3) and compared between KO mutants and WT.

(B) Representative images for top hits with dissolution and fusion defects. FlucSM-GFP aggregates are shown at 0 and 30 min after HS. Note *xrn1Δ* intensity is scaled differently than WT and other hits since the aggregates are dimmer.

Figure 2. Continued

(C and D) Normalized mean aggregate intensity (C) and normalized aggregate number per cell (D) of FlucSM-GFP labeled aggregates in KO strains after HS. Time represents the number of minutes after shifting back to permissive temperature. Error bars represent the SD (WT $n = 3$ movies and 165 cells, *hsp104Δ* $n = 3$ movies and 141 cells, *pfk1Δ* $n = 2$ movies and 90 cells, *sse1Δ* $n = 3$ movies and 91 cells, *xrn1Δ* $n = 3$ movies and 87 cells).

(E and F) Lineage trace (F) of *xrn1Δ* FlucSM-GFP labeled aggregates (top) and aggregate number (bottom) over time from time course images (E). Each line represents an aggregate track and the corresponding number of aggregates per cell at each time point. Due to the increased aggregate number per cell, only a subset of tracks are shown. Pink arrows represent events where a clustered aggregate falls apart. The color represents the mean intensity of the aggregate in the track; pink represents high intensity while blue represents low intensity aggregates.

(G and H) Lineage trace (H) of *pfk1Δ* FlucSM-GFP labeled aggregates (top) and aggregate number (bottom) over time from time course images (H). Only a subset of aggregate tracks are depicted. Statistically colored traces and arrow coloring same as in (E & F). Scale bar for all panels, 2 μm .

same cell or field of aggregates that were analyzed for FLIP, which showed minimal fluorescence decay during the FLIP experiment (Figures 1J and S1B). This data suggests that protein aggregates undergo SLPT within 30 min of recovery after HS.

To determine whether native aggregating proteins behave similarly to FlucSM and undergo SLPT during the dissolution process, we tested three native substrates (Ruan et al., 2017) that were highly enriched in protein aggregates: Ald6, Cdc19, and Sup45. These proteins colocalized with FlucSM aggregates 0 and 30 min after HS (Figure S1A) and the aggregates fused together during the recovery process (Figure S2D). Ald6 aggregates had the highest fluorescence intensity, enabling the application of FLIP analysis, which showed that Ald6-GFP shifted to having a higher mobile pool 30 min after HS in FLIP assays (Figures S1E–S1K), confirming that SLPT occurs also for native aggregated proteins.

Molecular regulators of protein disaggregation

We next sought to identify proteins that affect aggregate dissolution especially SLPT. We focused on 319 proteins previously detected in protein aggregates by mass spectrometry.⁴⁰ We reasoned that these proteins are enriched because they either are aggregation-prone proteins or regulate aggregate formation or dissolution. Among these, 97 mutants bearing knockout (KO) of a non-essential gene were tested for their effects on the dissolution of FlucSM aggregates (Figure 2A). All of these KO strains formed aggregates, indicating that none of the genes were required for aggregate formation. Given that SLPT and aggregate fusion occurred within 30 min in wild-type (WT) cells, we compared the fraction of aggregates remaining at 30 min relative to 0 min and the ranked ratio can be found in Table S1. Hits (*hsp104Δ*, *new1Δ*, *aro4Δ*, *pfk1Δ*, *alt2Δ*, *sse1Δ*, *his4Δ*, and *glk1*) were defined as mutants that had a ratio above 0.5, a value significantly higher than WT (Figures S3B and S3C). We also found mutants that had an increased aggregate number compared to WT at 0 min and 30 min (*xrn1Δ* and *sse1Δ*) (Figures 2B, S3C and S3D). Note that while *trp2Δ* had a significant increase in aggregate number at 0 min, the number was not significantly different than WT at 30 min (Figure S3D).

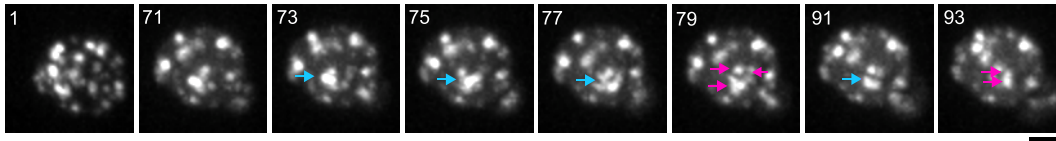
We validated these screen hits by quantifying aggregate intensity and number changes during dissolution (Figure S3), which confirmed that Hsp104, Xrn1, Sse1, and Pfk1 are important for aggregate dissolution and fusion. Xrn1 is a conserved 5' to 3' exonuclease⁴¹; Sse1 is a Hsp110 family chaperone^{42,43}; and Pfk1 is the alpha subunit of phosphofructokinase, a key glycolytic enzyme.⁴⁴ As shown previously,³⁵ aggregates in the *hsp104Δ* background failed to dissolve: the number and intensity of aggregates did not decrease over time (Figures 2C and 2D). *pfk1Δ* and *sse1Δ* cells exhibited a significantly longer half-time of aggregate fluorescence intensity and number compared to WT (Figure S3E). *xrn1Δ* exhibited a slower decline in aggregate number compared to WT but the normalized fluorescence intensity decrease was more similar to WT (Figures 2C, 2D, S3D, and S3E), suggesting that Xrn1 may play a role in the fusion of aggregates rather than dissolution. Of the remaining strains that had a ratio above 0.5 (Figure S3C), aggregates in *alt2Δ*, *aro4Δ*, *glk1Δ*, *his4Δ*, and *new1Δ* strains dissolved and were able to fuse during dissolution (Figures S3B, S3F, and S3G). *alt2Δ*, deleted of a catalytically inactive transaminase,⁴⁵ showed a significant delay in the reduction in aggregate number but not intensity, although aggregates were able to fuse together and dissolve within 150 min (Figures S3E, S3H, and S3I).

Hsp104 is required for solid-to-liquid phase transition

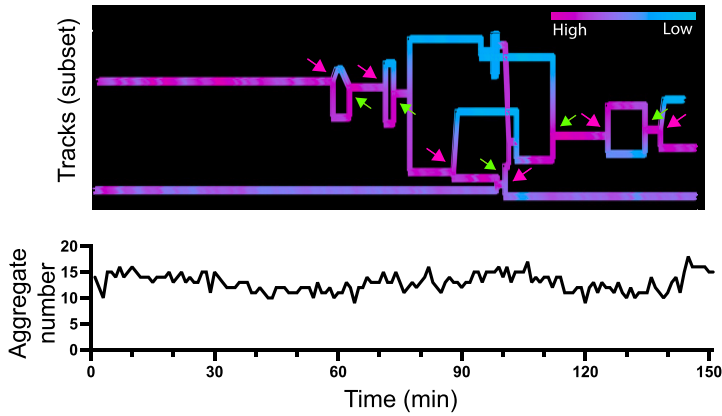
Hsp104 was the most prominent hit in the above screen. Consistently, Hsp104 was previously shown to be required for the dissolution of protein aggregates (Zhou et al., 2011; Glover and Lindquist, 1998). We next investigated whether Hsp104 was required for SLPT or subsequent aggregate dissolution, or both. We observed that aggregates in *hsp104Δ* were mobile and often cluster transiently without fusion and remained jagged rather than became round like those in WT (Figures 3A–3D, Video S2). Average aggregate intensity increased in *hsp104Δ* cells, as more misfolded proteins accumulated in the absence of Hsp104 even in the absence of continued stress, which was likely due to the time it takes for cells to recover normal protein folding capacity. FLIP assay showed that there was little molecular diffusion in aggregates in the *hsp104Δ* background even after 30 min recovery (Figures 3D–3F). The immobile fraction did not defer significantly between 0 and 30 min after HS (Figure 3G). These observations suggest that Hsp104 is required for SLPT during aggregate dissolution.

It was possible that in the *hsp104Δ* background aggregates that formed had an altered molecular organization that prevented SLPT. We therefore tested whether the induction of Hsp104 expression after HS could rescue the SLPT defect in *hsp104Δ* cells. Hsp104 expression was induced with the β -estradiol-inducible system⁴⁶ after heat shock in *hsp104Δ* cells (schematic in Figure 3H). Inducing Hsp104 expression in *hsp104Δ* not only rescued dissolution, clearing cytoplasmic aggregates in 3 h (Figures 3I and 3G), but it also rescued SLPT (Figures 3K, 3L, S4B, and S4C). This suggests that Hsp104 promotes SLPT of aggregates formed in the absence of HSP104. Together, these data support the conclusion that Hsp104 is required for SLPT.

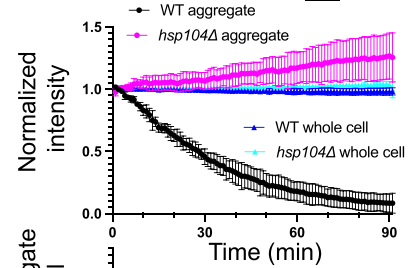
A FlucSM-GFP *hsp104Δ*



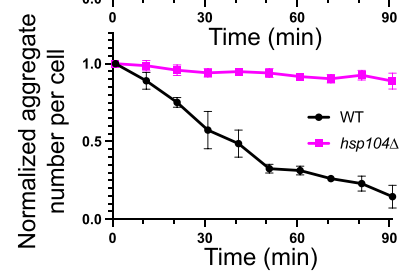
B



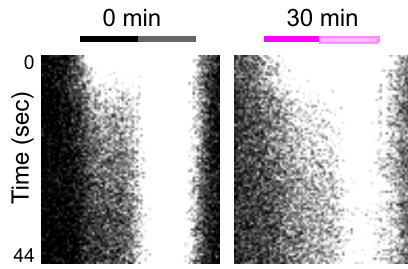
C



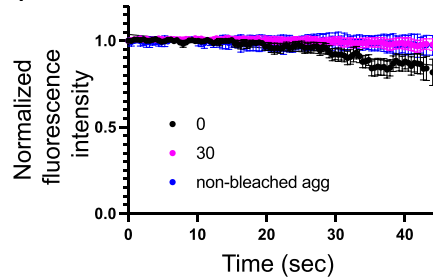
D



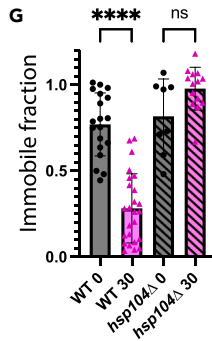
E *hsp104Δ*



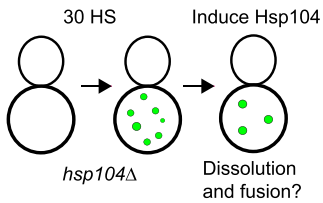
F



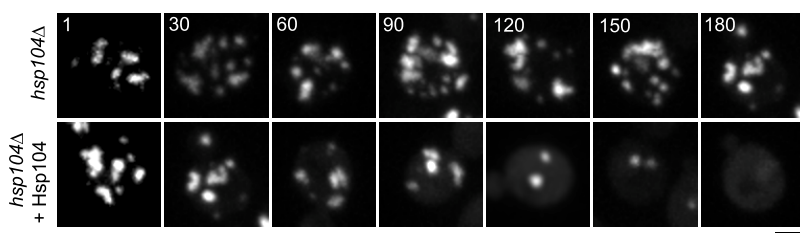
G



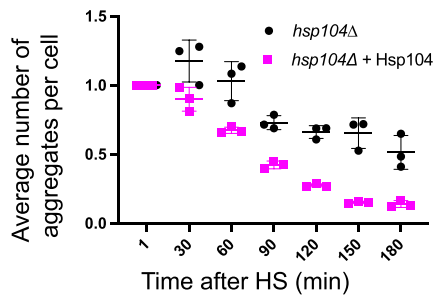
H



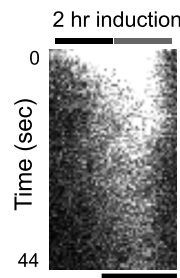
I



J



K



L

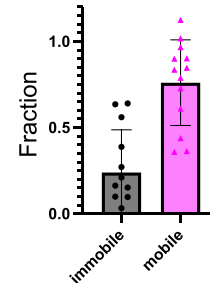


Figure 3. Hsp104 is required for the solid to liquid-like transition

- (A) Dissolution of FlucSM-GFP labeled aggregates in *hsp104Δ* cells during a 90 min time course showing not only failure for aggregates to dissolve, but also lack of fusion. Pink arrows indicate individual aggregates and teal arrows aggregates that cluster together but do not stay together. Scale bar, 2 μm.
- (B) Lineage trace and aggregate number over time for images in (A). Pink arrows represent events where a clustered aggregate moves apart and green arrows represent when they come together. The color represents the mean intensity of the aggregate in the track; pink represents high intensity while blue represents low intensity aggregates.
- (C and D) Normalized mean whole cell and aggregate intensity (C) and normalized aggregate number per cell (D) of FlucSM-GFP labeled aggregates following HS. Time represents the number of min after shifting back to permissive temperature of 30°C (WT n = 3 movies and 96 cells and *hsp104Δ* n = 3 movies and 110 cells). Error bars represent SD. Images were taken alongside and compared to WT from Figure 1D.
- (E) Representative FLIP kymograph of a FlucSM-GFP labeled aggregate in *hsp104Δ* cells 0 and 30 min after HS. For 0 min after HS: the bleached region (black line) and non-bleached region (gray line). For 30 min after HS: the bleached region (pink line) and non-bleached region (light pink line) and the fluorescence loss in these two examples is quantified in (Figures S4G–S4J). Scale bar, 1 μm.
- (F) Mean normalized aggregate intensity and SEM for FLIP experiments (n = 8 for *hsp104Δ* 0 min, and n = 14 for *hsp104Δ* 30 min). Control normalized fluorescence intensity of a non-bleached aggregate in the same field as the bleached aggregates at 0 min time point in *hsp104Δ* cells (n = 8 aggregates).
- (G) Immobile fraction in *hsp104Δ* cells compared to WT (Figure 1) and error bars represent SD. Individual data points represent the immobile fraction of a single non-bleached aggregate half. Statistical analysis was performed via a one-way ANOVA with a p value < 0.05 followed by a Tukey post hoc test with the following significance cut-off: not significant (ns): p > 0.05, *: p ≤ 0.05, **: p ≤ 0.01, ***: p ≤ 0.001, ****: p ≤ 0.0001.
- (H) Schematic of Hsp104 induction experiment in *hsp104Δ* background.
- (I) Aggregates were allowed to form in the absence of Hsp104 and Hsp104 expression was induced with estradiol (ethanol as a solvent control) and images from 30 min time intervals after HS. Scale bar, 2 μm. Note the intensity is scaled differentially for t = 1 to prevent overexposure of following images.
- (J) Mean aggregate number per cell decreases with the induction of Hsp104 expression in *hsp104Δ*. Each dot represents the average number of aggregates per cell in one field (n = 3 fields each). Error bars represent the SD.
- (K and L) Representative FLIP kymograph of *hsp104Δ* cells induced with Hsp104 expression for 2 h with estradiol (K) and quantification of the mobile vs. immobile fraction (L) (n = 13 aggregates). Scale bar, 1 μm.

Hsp104 chaperone activity is required for solid-to-liquid phase transition

Hsp104 is a molecular chaperone that requires both substrate binding and ATPase activity to dissolve protein aggregates.¹⁸ To determine which or both Hsp104 activities are required for SLPT, we examined aggregate dissolution, fusion, and SLPT in cells that expressed a Hsp104 variant defective in substrate binding (Hsp104^{Y257A})^{24,26} or ATP hydrolysis (Hsp104^{DWB})²⁶ or a potentiated variant with a missense mutation in helix 3 that enhances aggregate dissolution *in vitro* and suppresses proteotoxicity induced by WT TDP-43, FUS, and α-synuclein (Hsp104^{A503V}) (Jackrel et al., 2014; Tariq et al., 2018) in the *hsp104Δ* background (Figure 4A). We found that aggregates labeled with FlucSM-GFP in the *hsp104* mutant defective in substrate binding or ATP hydrolysis not only did not dissolve but also did not fuse (Figures 4B–4D). FLIP assays confirmed that aggregates in *hsp104*^{Y257A} and *hsp104*^{DWB} mutants remained solid-like even after a 30 min recovery (Figures 4E–4J). Surprisingly, aggregates dissolved moderately, but not significantly, slower than WT in cells that expressed the potentiated variant Hsp104^{A503V} (Figures 4C, S4D, and S4E). The fluorescence intensity of aggregates was on average 3x brighter in *hsp104*^{A503V} cells compared to WT (Figure S4L). FLIP assay showed that SLPT also occurred in this potentiated mutant during dissolution (Figures 4E–4J). This data suggests that the chaperone activity of Hsp104 is required for SLPT of protein aggregates *in vivo*.

Hsp104 is known to function with Hsp70 chaperones (Tessarz, Mogk and Bukau, 2008, 2008; Glover and Lindquist, 1998). SSA1, SSA2, SSA3 and SSA4 encode the yeast Hsp70 proteins that function to assist Hsp104 in disaggregation and refolding.^{47–49} Ssa1, Ssa2, and Ssa3 were enriched in aggregates; however, the single KO mutants did not exhibit a dissolution defect (Figures S5A–S5C). To test the combined effects of disrupting these Hsp70 proteins, we compared aggregate dissolution between the *ssa1^{ts} ssa2Δ ssa3Δ ssa4Δ* quadruple mutant⁴² to WT and *hsp104Δ*. FlucSM-GFP aggregates in the *ssa1^{ts} ssa2Δ ssa3Δ ssa4Δ* mutant background were able to fuse and dissolve, albeit slower than WT (Figures 5A–5D). FLIP assay showed a significant difference in the immobile fraction from 0 to 30 min in *ssa1^{ts} ssa2Δ ssa3Δ ssa4Δ* mutant cells (Figures 5E, 5G, 5H, and 5J), suggesting that SLPT occurred in this mutant. However, only 65% of aggregates exhibited high diffusion in *ssa1^{ts} ssa2Δ ssa3Δ ssa4Δ* cells; in comparison, 88% of WT cells did so after a 30 min recovery, although the immobile fraction was not significantly different between the aggregates that had higher molecular mobility (Figures S5F and S5G).

Sse1, identified as a hit in our screen, is the nucleotide exchange factor for the Hsp70 chaperones. Sse1 cells showed a similar decrease in average aggregate intensity after HS to *ssa1^{ts} ssa2Δ ssa3Δ ssa4Δ*, but the decline in aggregate number occurred more slowly (Figures 5A–5D). This could be a result of aggregate fusion being impaired, as observed through time-lapse microscopy (Figure 5A). FLIP assay showed that *sse1Δ* aggregates did not undergo SLPT (Figures 5F and 5I–5J), as there was not a significant difference in the immobile pool between 0 and 30 min. Sse1 is also a co-chaperone of Hsp90, yet Hsc82, the main cytoplasmic Hsp90 in yeast, did not have a dissolution defect in our screen (Figures S5B and S5C). These data suggest that Hsp70 proteins may not be required for SLPT but are important for aggregate dissolution, whereas Sse1 plays an important role in SLPT independent of its function with Hsp70 or Hsp90 chaperones.

Hsp104 is required also for aggregate dissolution after solid-to-liquid phase transition

Finally, we investigated whether Hsp104 is continuously required for aggregate dissolution after SLPT. In this experiment, aggregates were allowed to form in WT cells under HS; Hsp104 activity was then inhibited with guanidine hydrochloride (GdnHCl)^{50–53} either immediately after HS, when aggregates were solid, or after a 30 min recovery, when aggregates had mostly undergone SLPT (Figures 4A and 4B). As expected, inhibiting Hsp104 right after the formation of aggregates phenocopied *hsp104Δ* (Figure 6A). Whole cell FlucSM-GFP levels did not increase

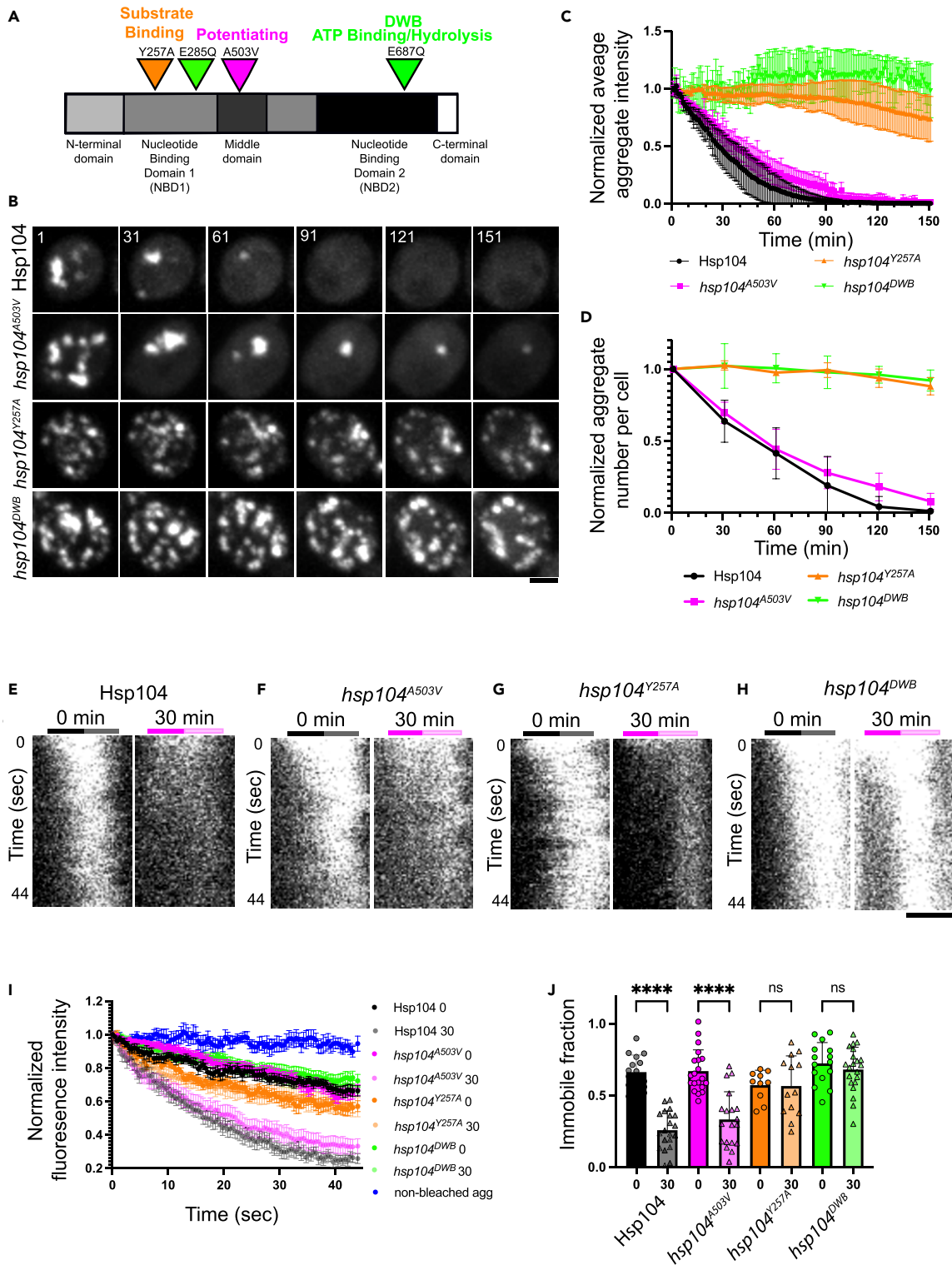


Figure 4. Hsp104 activity is required for the solid to liquid-like transition after HS

(A) Schematic of Hsp104 and point mutations that affect chaperone activity that are used in our study. Color labels are consistent for these mutants in graphs C, D, I, and J.

(B) Montages of FlucSM-GFP labeled aggregates in cells with indicated Hsp104 mutations recovering from HS over 150 min time lapse movie. Scale bar, 2 μ m.

Figure 4. Continued

(C and D) Normalized mean aggregate intensity (C) and normalized aggregate number per cell (D) of FlucSM-GFP labeled aggregates following HS. Error bars represent SD. (Hsp104 WT $n = 3$ movies and 132 cells, *hsp104*^{AS03V} $n = 3$ movies and 132 cells, *hsp104*^{Y257A} $n = 3$ movies and 146 cells, and *hsp104*^{DWB} $n = 3$ movies and 143 cells).

(E and H) Representative kymographs of FlucSM-GFP labeled aggregates in Hsp104 variant backgrounds at 0 min and 30 min after HS in cells expressing WT Hsp104 (E), Hsp104^{AS03V} (F), Hsp104^{Y257A} (G), Hsp104^{DWB} (H). For 0 min after HS: the bleached region (black line) and non-bleached region (gray line). For 30 min after HS: the bleached region (pink line) and non-bleached region (light pink line).

(I) Normalized mean aggregate intensity and SEM for FLIP experiments acquired in cells expressing WT Hsp104 ($n = 15$ and 20), Hsp104^{AS03V} ($n = 20$ and 19), Hsp104^{Y257A} ($n = 10$ and 13), and Hsp104^{DWB} ($n = 21$ and 15) 0 and 30 min after HS. Scale bar, 0.5 μm . Control normalized fluorescence intensity of a non-bleached aggregate in the same field as bleached aggregates at 0 min time point in WT Hsp104 cells ($n = 8$ aggregates).

(J) Immobile fraction from the non-bleached half from FLIP experiments. Individual data points represent a single non-bleached aggregate half. Statistical analysis was performed via a one-way ANOVA with a p value < 0.05 followed by a Tukey post hoc test with the following significance cut-off: not significant (ns): $p > 0.05$, *: $p \leq 0.05$, **: $p \leq 0.01$, ***: $p \leq 0.001$, ****: $p \leq 0.0001$.

with GdnHCl treatment (Figure S4N). Interestingly, inhibiting Hsp104 at 30 min after HS prevented the dissolution of aggregates even after SLPT (Figures 6B and 6D). FLIP experiments confirmed that these remaining aggregates remained in the liquid-like state after treatment with GdnHCl for 60 min (Figures 6E–6I). This data suggests that Hsp104 is required for both SLPT and the subsequent dispersal of the protein aggregates from the liquid-like state. Hsp104 inhibition with GdnHCl treatment was reversible and upon removal of the drug, aggregates were able to be dissolved as aggregate number decreased over time, albeit slower than WT (Figure S4O).

DISCUSSION

In this work, we established the steps involved in the dissolution of solid protein aggregates after acute heat stress, although it does not appear that these steps are strictly temporally separated. First, the solid aggregates cluster together. Second, the clustered aggregates undergo SLPT driven by the chaperone action of Hsp104, which allows the aggregates to fuse and reduce in number. Lastly, the liquid-like condensates complete dissolution in an Hsp104 chaperone-dependent manner.

Disease mutations in prion-like proteins such as Fused in Sarcoma (FUS) or polyglutamine expansions in the Huntingtin protein shift from liquid-like to solid-like condensates with fibrillar structures.^{13,14,54} Similar phenomena are also observed with tau¹⁵ and α -synuclein,¹⁶ which are implicated in Alzheimer's disease and Parkinson's disease, respectively. These studies suggested a link between changes in the phase property of protein aggregates and disease progression. Our findings suggest that the dissolution of solid protein aggregates can go through a reverse process involving SLPT and a liquid-phase intermediate. Several previous studies showed that protein aggregates in yeast are able to fuse but did not characterize the molecular changes that enabled fusion.^{35,36} SLPT makes the subsequent fusion a spontaneous process. While our results indicated that the observed SLPT is not limited to aggregates of the model substrate FlucSM, it will be interesting to investigate if a similar process applies to the dissolution of aggregates formed under other types of stress or in metazoan organisms.

By screening the effects of KO mutants affecting components of the HS-induced protein aggregates, we identified several proteins that play roles in aggregate dissolution. The most prominent hit was Hsp104; the yeast cytosolic disaggregase. It was surprising, however, that Hsp104 is required for the SLPT step in aggregate dissolution as well as the subsequent dispersal of the liquid condensate. Structural and biochemical studies led to the model that Hsp104 disaggregates by threading misfolded polypeptide through its hexamer ring.^{23,55} It is possible that the resulting unfolded polypeptides exhibit low-affinity interactions with each other and the ionic environment to form a liquid-like state. Another possibility is that the unthreading activity of Hsp104 helps order misfolded proteins into a liquid crystal-like arrangement. This ordering would be energetically favorable if the hydrophobic domains of misfolded proteins align within the liquid crystal. A recent study in human cells observed anisotropic liquid crystal structures formed with nuclear TDP-43, which is dependent on HSP70s for maintenance.⁵⁶

Ostwald ripening may underlie the growth of the liquid-like protein aggregates when larger aggregates get larger at the expense of smaller aggregates. This is a very interesting concept, however it is difficult to determine experimentally as our system is dissipative. Not only are protein aggregates undergoing an SLPT during dissolution, but proteins are also being refolded and degraded. In our experimental conditions, FlucSM-GFP levels remained largely constant during the SLPT (Figures 1E, S1F and S1G) as protein aggregates are being refolded, degraded, and new protein is synthesized. Our previous study showed that FlucSM-GFP can be degraded by the mitochondria-associated MAGIC pathway and proteasomes.⁴⁰ Degradation was apparent only in the presence of cycloheximide with kinetics slower than dissolution. More work is needed to understand how the disaggregation of misfolded proteins and their phase properties are connected to and contribute to downstream processes such as degradation and refolding.

While Hsp104 was the major hit in our screen, we also identified several other regulators of aggregate dissolution such as Xrn1, Pfk1, and Sse1. Sse1, an HSP110 family chaperone, is a nucleotide exchange factor that loads ATP onto the SSA family of HSP70s.^{42,43} Its role in aggregate dissolution is in line with our observation that the *ssa1-4* quadruple mutant showed a strong dissolution defect. In addition to its function with Hsp70s, Sse1 is also the ATPase component of Hsp90s. Hsc82, the chaperone of the Hsp90 family, is enriched in aggregates, yet did not have a dissolution defect in our screen. A recent study suggests that Sse1 may help recruit Hsp104 to protein aggregates independently of its ability to interact with Hsp70,⁵⁷ and this could possibly explain Sse1's role in SLPT. HSP70 and their HSP110 family co-chaperones have been implicated in the dissolution of protein aggregates in mammalian cells, and it will be interesting to investigate whether the role in SLPT is a conserved function.^{29,30,32,33,56,58}

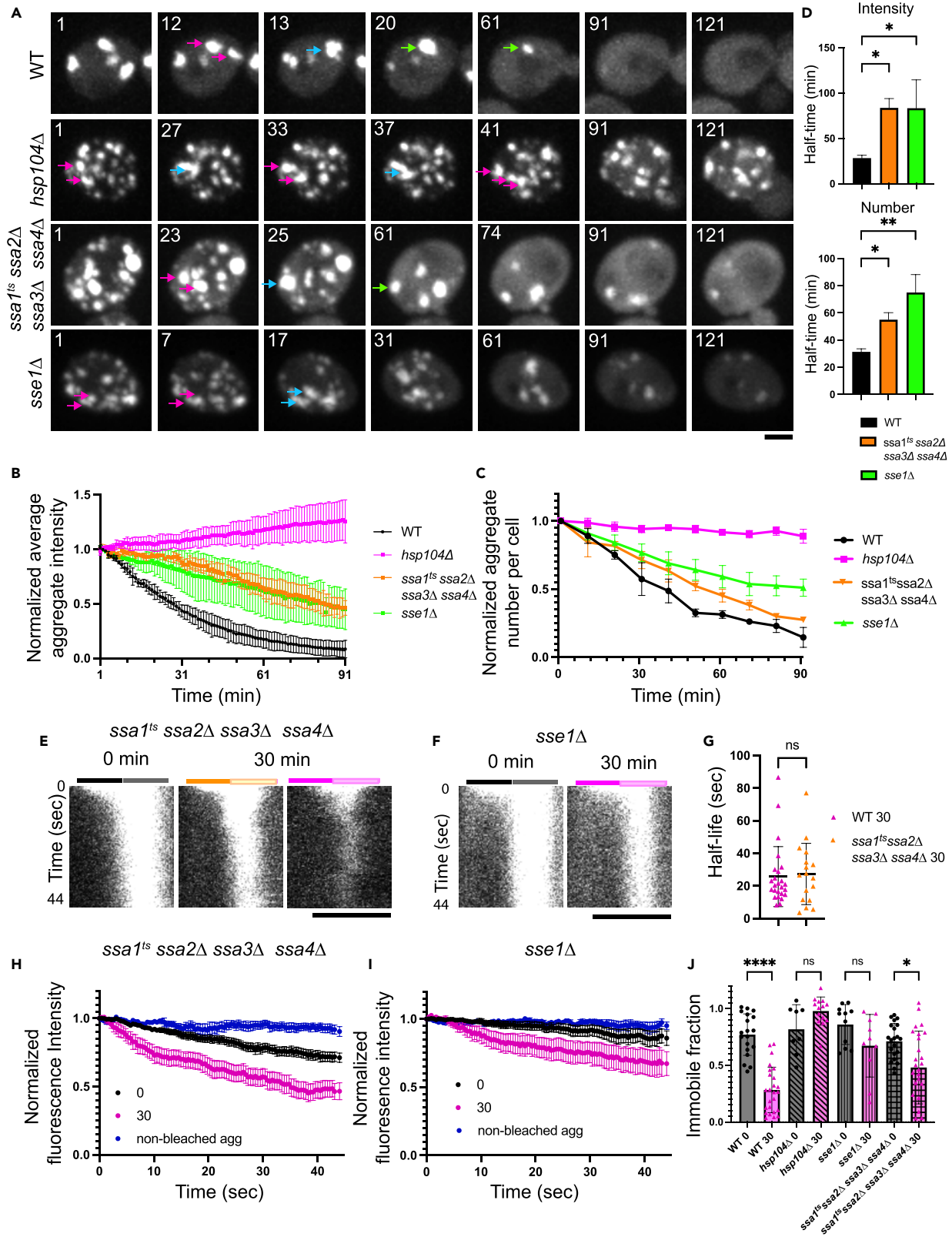


Figure 5. The role of Hsp70 chaperones in aggregate dissolution

(A) Time-lapse images of FlucSM-GFP labeled aggregates in cells in indicated strain backgrounds over 2 h. Scale bar, 2 μ m.

(B and C) Normalized mean aggregate intensity (B) and normalized aggregate number per cell (C) of FlucSM-GFP labeled aggregates following HS. Error bars represent SD. (WT n = 3 movies and 96 cells, *hsp104 Δ* n = 3 movies and 110 cells, the *ssa1^{ts} ssa2 Δ ssa3 Δ ssa4 Δ* n = 3 movies and 91 cells, *sse1 Δ* n = 3 movies and 91 cells). *ssa1^{ts} ssa2 Δ ssa3 Δ ssa4 Δ* plotted alongside WT (Figure 1), *sse1* (Figure 2), and *hsp104* (Figure 3).

(D) Half-time of aggregate dissolution for aggregate number and intensity. Statistical analysis was performed via a one-way ANOVA with a p value < 0.05 followed by a Tukey post hoc test with the following significance cut-off: not significant (ns): p > 0.05, *: p \leq 0.05, **: p \leq 0.01, ***: p \leq 0.001, ****: p \leq 0.0001.

(E and F) Kymographs of bleached aggregates for FLIP experiments in *ssa1^{ts} ssa2 Δ ssa3 Δ ssa4 Δ* (E) and *sse1 Δ* (F). Scale bar is 1 μ m.

(H and I) Normalized fluorescence intensity for FLIP experiments (H) and (I) respectively. (*ssa1^{ts} ssa2 Δ ssa3 Δ ssa4 Δ* n = 21 and n = 26 for 0 and 30 and for *sse1 Δ* n = 11 and n = 10 for 0 and 30). Control normalized fluorescence intensity of a non-bleached aggregate in the same field as bleached aggregates at 0 min time point in *ssa1^{ts} ssa2 Δ ssa3 Δ ssa4 Δ* cells (H, n = 14 aggregates) and *sse1 Δ* cells (I, n = 11 aggregates).

(G and J) Half-life (G) and immobile fraction (J) plotted alongside WT (Figure 1) and *hsp104 Δ* (Figure 3). Statistical analysis was performed via an unpaired two-tailed t-test (G) and a one-way ANOVA (J) with the same significance cut-offs as in (D).

Xrn1 is the major 5' to 3' exonuclease in the cytoplasm and is highly conserved. *xrn1 Δ* cells formed many small aggregates after HS that did not fuse together, yet they were able to dissolve. However, as these aggregates were small and dim, it was technically not possible to probe their dynamics in an FLIP assay. A study showed that in *C. elegans* embryos, Pacman/Xrn1 and other decapping factors help cluster mRNAs and may have a similar role in germ granules.⁵⁹ The fact that Xrn1 is enriched in aggregates and has a role in aggregate dynamics suggests that there may be RNA in our aggregates that could contribute to their phase behavior. This is supported by the fact that there are many RNA binding proteins enriched in aggregates⁴⁰ and that the formation of aggregates is dependent upon active translation.³⁸

The role of Pfk1, the alpha subunit of phosphofructokinase, in aggregate dissolution may be explained by its enzymatic role in glycolysis, which we previously showed to be the main process that produced ATP for cytosolic aggregate dissolution.³⁸ Pfk2, the beta subunit of phosphofructokinase, has been shown to be required for glucose starvation induced aggregate dissolution in a PKA-dependent manner.⁶⁰ Supporting this, 9 out of 15 glycolytic enzymes were found to be enriched in aggregates.⁴⁰ It is possible that concentrating glycolytic enzymes in protein aggregates provides mechanism for the localized ATP production to fuel chaperone-mediated aggregate dissolution, as the ATP hydrolysis activity of Hsp104 is one factor that can regulate aggregate number and size.⁶⁰ In addition, a high local concentration of ATP could serve as a hydrotrope as previously proposed⁶¹ to directly facilitate aggregate dissolution.

Limitations of the study

Our main conclusion that protein aggregates formed after HS undergo an SLPT after stress attenuation which is dependent upon Hsp104, was mainly based on genetic analysis and imaging-based methods. *In vitro* biochemical methods, especially one that could enable the direct assessment of the activity of Hsp104 in the SLPT and dissolution process, should provide additional evidence and insight. In addition, our work is limited to yeast cells. Future work in other cell types and species should shed light on the generality of our findings of a solid-to-liquid phase transition in the dissolution of misfolded protein aggregates.

STAR★METHODS

Detailed methods are provided in the online version of this paper and include the following:

- KEY RESOURCES TABLE
- RESOURCE AVAILABILITY
 - Lead contact
 - Materials availability
 - Data and code availability
- EXPERIMENTAL MODEL AND STUDY PARTICIPANT DETAILS
 - Yeast *saccharomyces cerevisiae*
- METHOD DETAILS
 - Microscopy
 - Aggregate dissolution assays
 - Aggregate subset screen
 - FLIP experiments
 - Photoconversion
 - Circularity
 - Lineage tracing
 - Immunoblot analysis
 - Drug treatments
- QUANTIFICATION AND STATISTICAL ANALYSIS
 - Statistical analysis

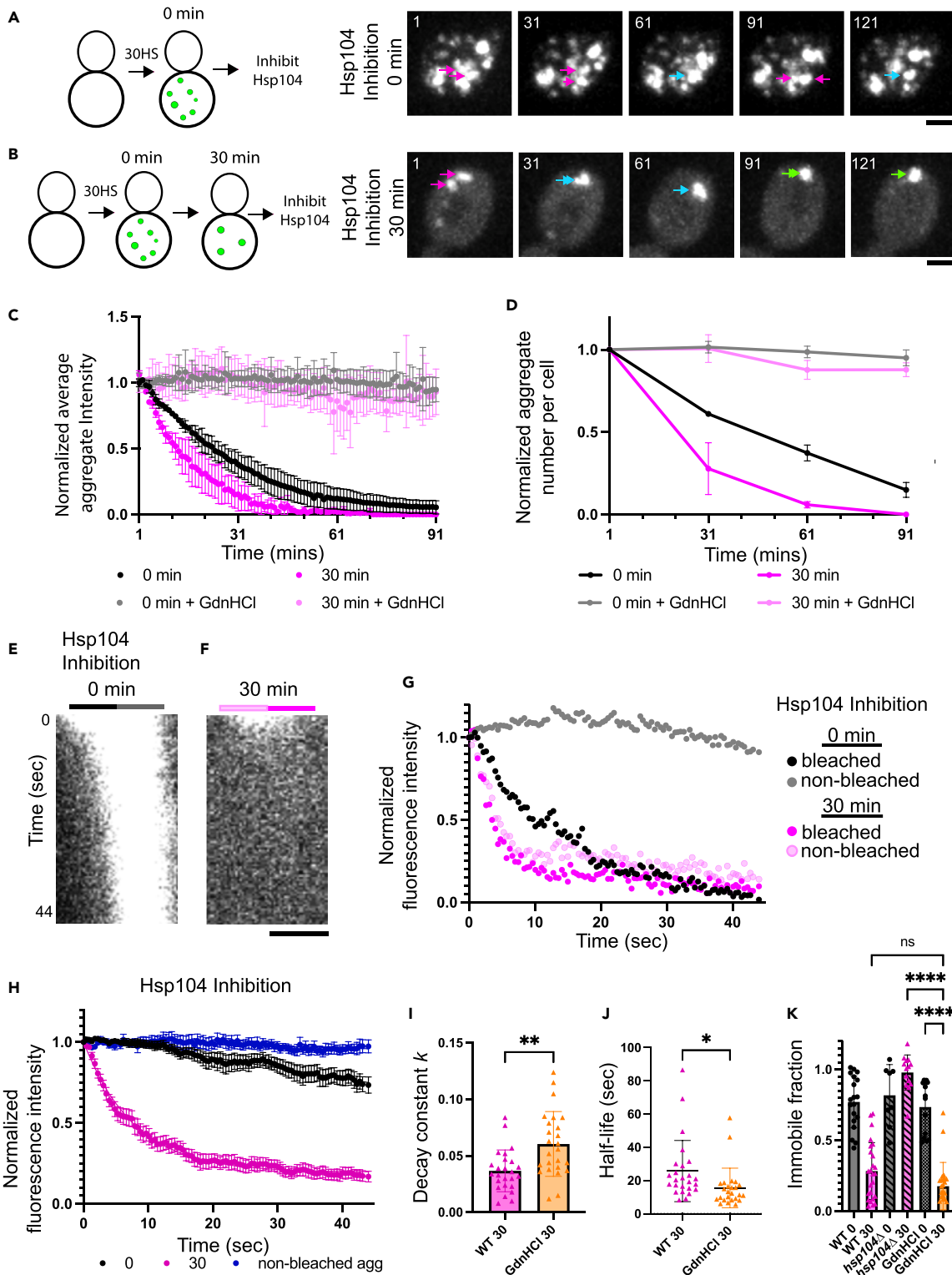


Figure 6. Aggregates must first undergo a Hsp104 dependent phase transition before dissolution

(A) Schematic illustrating that aggregates were allowed to form in WT cells, and 0 min after HS, Hsp104 was inhibited with GdnHCl. Representative maximum intensity projection images are shown every 30 min. Scale bar, 2 μ m. Pink arrows represent individual aggregates and teal arrows aggregates that cluster together.

Figure 6. Continued

(B) Same as (A) but Hsp104 was inhibited 30 min after HS.

(C and D) Average aggregate intensity does not decrease with Hsp104 inhibition when added at either time point (C) nor does the normalized aggregate number per cell with Hsp104 inhibition (D) (WT 0 min $n = 2$ and 110 cells, 0 min + GdnHCl $n = 3$ and 140 cells, WT 30 min $n = 2$ and 106 cells, and 30 min + GdnHCl $n = 3$ and 114 cells).

(E and F) Representative FLIP kymograph of a FlucSM-GFP labeled aggregate when Hsp104 was inhibited with GdnHCl for 1 h after 0 min (E) and 30 min after HS (F). For 0 min after HS: the bleached region (black line) and non-bleached region (gray line). For 30 min after HS: the bleached region (pink line) and non-bleached region (light pink line). Scale bar, 0.5 μm .

(G) Quantification of the fluorescent loss of the bleached half and non-bleached half of aggregates in (E&F).

(H) Normalized mean aggregate intensity and SEM for FLIP experiments acquired in cells with Hsp104 inhibited 0 min and 30 min after HS ($n = 14$ and $n = 25$ respectively). Control normalized fluorescence intensity of a non-bleached aggregate in the same field as bleached aggregates at 0 min time point in cells inhibited with GdnHCl at 0 min ($n = 10$ aggregates).

(I–K) Decay rate k (I), half-life (J), and immobile fraction (K) from the non-bleached half from FLIP experiments compared to WT and *hsp104 Δ* . Individual data point represent a single bleached aggregate and statistical analysis was performed via an unpaired two-tailed t-test (I–J) and a one-way ANOVA (K) with the following significance cut-off: not significant (NS): $p > 0.05$, *: $p \leq 0.05$, **: $p \leq 0.01$, ***: $p \leq 0.001$, ****: $p \leq 0.0001$.

SUPPLEMENTAL INFORMATION

Supplemental information can be found online at <https://doi.org/10.1016/j.isci.2023.108334>.

ACKNOWLEDGMENTS

We thank James Shorter (University of Pennsylvania) for the Hsp104 variant plasmids, Bin Wu (Johns Hopkins Medicine) for the TetraSpeck fluorescent beads, Geraldine Seydoux, Susan Michaelis, Yuhao Wang, Abhijit Deb Roy, Josh McNamara, Molly Gordon, Linhao Ruan, Gordon Sun, and Blake Johnson (Johns Hopkins University School of Medicine) for valuable input throughout the project.

Funding

This work was funded initially from a grant from the National Institutes of Health (USA) and subsequently a grant from ReStem Biotech to RL, and a Research Center of Excellence grant from the Ministry of Education (Singapore) that supported collaborative efforts from the Mechanobiology Institute. J.L. was supported by start-up funds from the Johns Hopkins University School of Medicine, Johns Hopkins Catalyst award, the National Science Foundation (2105837 and 2148534), and National Institutes of Health (1RO1 GM148459-01).

AUTHOR CONTRIBUTIONS

A.T. and R.L. conceived the study and designed experiments. A.T. performed the experiments and imaging analysis. J.Z. contributed to the screen design and execution. R.W. performed the imaging for the screen. E.S. facilitated FLIP data analysis. J.L. provided advice on experimental design and data analysis. A.T. and R.L. wrote the article; J.Z., Y.W., J.M., and J.L. edited the article. R.L. supervised the project.

DECLARATION OF INTERESTS

The authors declare no competing interests.

Received: June 2, 2023

Revised: September 8, 2023

Accepted: October 22, 2023

Published: October 28, 2023

REFERENCES

1. Powers, E.T., Morimoto, R.I., Dillin, A., Kelly, J.W., and Balch, W.E. (2009). Biological and Chemical Approaches to Diseases of Proteostasis Deficiency. *Annu. Rev. Biochem.* 78, 959–991. <https://doi.org/10.1146/annurev.biochem.052308.114844>.
2. Doyle, S.M., Genest, O., and Wickner, S. (2013). Protein rescue from aggregates by powerful molecular chaperone machines. *Nat. Rev. Mol. Cell Biol.* 14, 617–629. <https://doi.org/10.1038/nrm3660>.
3. Hartl, F.U. (2017). Protein Misfolding Diseases. *Annu. Rev. Biochem.* 86, 21–26. <https://doi.org/10.1146/annurev-biochem-061516-044518>.
4. Jayaraj, G.G., Hipp, M.S., and Hartl, F.U. (2020). Functional Modules of the Proteostasis Network. *Cold Spring Harbor Perspect. Biol.* 12, a033951. <https://doi.org/10.1101/cshperspect.a033951>.
5. López-Otín, C., Blasco, M.A., Partridge, L., Serrano, M., and Kroemer, G. (2013). The Hallmarks of Aging. *Cell* 153, 1194–1217. <https://doi.org/10.1016/j.cell.2013.05.039>.
6. Knowles, T.P.J., Vendruscolo, M., and Dobson, C.M. (2014). The amyloid state and its association with protein misfolding diseases. *Nat. Rev. Mol. Cell Biol.* 15, 384–396. <https://doi.org/10.1038/nrm3810>.
7. Valastyan, J.S., and Lindquist, S. (2014). Mechanisms of protein-folding diseases at a glance. *Dis. Model. Mech.* 7, 9–14. <https://doi.org/10.1242/dmm.013474>.
8. Jarosz, D.F., and Khurana, V. (2017). Specification of Physiologic and Disease States by Distinct Proteins and Protein Conformations. *Cell* 171, 1001–1014. <https://doi.org/10.1016/j.cell.2017.10.047>.
9. Hipp, M.S., Park, S.-H., and Hartl, F.U. (2014). Proteostasis impairment in protein-misfolding and -aggregation diseases. *Trends Cell Biol.* 24, 506–514. <https://doi.org/10.1016/j.tcb.2014.05.003>.
10. Dugger, B.N., and Dickson, D.W. (2017). Pathology of Neurodegenerative Diseases. *Cold Spring Harbor Perspect. Biol.* 9, a028035. <https://doi.org/10.1101/cshperspect.a028035>.
11. Sweeney, P., Park, H., Baumann, M., Dunlop, J., Frydman, J., Kopito, R., McCampbell, A., Leblanc, G., Venkateswaran, A., Nurmi, A., and Hodgson, R. (2017). Protein misfolding in neurodegenerative diseases: implications

- and strategies. *Transl. Neurodegener.* 6, 6. <https://doi.org/10.1186/s40035-017-0077-5>.
12. Hyman, A.A., Weber, C.A., and Jülicher, F. (2014). Liquid-Liquid Phase Separation in Biology. *Annu. Rev. Cell Dev. Biol.* 30, 39–58. <https://doi.org/10.1146/annurev-cellbio-100913-013325>.
 13. Patel, A., Lee, H.O., Jawerth, L., Maharana, S., Jahnel, M., Hein, M.Y., Stoynov, S., Mahamid, J., Saha, S., Franzmann, T.M., et al. (2015). A Liquid-to-Solid Phase Transition of the ALS Protein FUS Accelerated by Disease Mutation. *Cell* 162, 1066–1077. <https://doi.org/10.1016/j.cell.2015.07.047>.
 14. Peskett, T.R., Rau, F., O'Driscoll, J., Patani, R., Lowe, A.R., and Saibil, H.R. (2018). A Liquid to Solid Phase Transition Underlying Pathological Huntingtin Exon1 Aggregation. *Mol. Cell* 70, 588–601.e6. <https://doi.org/10.1016/j.molcel.2018.04.007>.
 15. Kanaan, N.M., Hamel, C., Grabinski, T., and Combs, B. (2020). Liquid-liquid phase separation induces pathogenic tau conformations in vitro. *Nat. Commun.* 11, 2809. <https://doi.org/10.1038/s41467-020-16580-3>.
 16. Ray, S., Singh, N., Kumar, R., Patel, K., Pandey, S., Datta, D., Mahato, J., Panigrahi, R., Navalkar, A., Mehra, S., et al. (2020). α -Synuclein aggregation nucleates through liquid-liquid phase separation. *Nat. Chem.* 12, 705–716. <https://doi.org/10.1038/s41557-020-0465-9>.
 17. Weids, A.J., Ibstedt, S., Tamás, M.J., and Grant, C.M. (2016). Distinct stress conditions result in aggregation of proteins with similar properties. *Sci. Rep.* 6, 24554. <https://doi.org/10.1038/srep24554>.
 18. Glover, J.R., and Lindquist, S. (1998). Hsp104, Hsp70, and Hsp40: A Novel Chaperone System that Rescues Previously Aggregated Proteins. *Cell* 94, 73–82. [https://doi.org/10.1016/S0092-8674\(00\)81223-4](https://doi.org/10.1016/S0092-8674(00)81223-4).
 19. Goloubinoff, P., Mogk, A., Zvi, A.P., Tomoyasu, T., and Bukau, B. (1999). Sequential mechanism of solubilization and refolding of stable protein aggregates by a bichaperone network. *Proc. Natl. Acad. Sci. USA* 96, 13732–13737. <https://doi.org/10.1073/pnas.96.24.13732>.
 20. Hartl, F.U., Bracher, A., and Hayer-Hartl, M. (2011). Molecular chaperones in protein folding and proteostasis. *Nature* 475, 324–332. <https://doi.org/10.1038/nature10317>.
 21. Parsell, D.A., Singer, M.A., and Lindquist, S. (1994). Protein disaggregation mediated by heat-shock protein Hsp104. *Nature* 372, 475–478. <https://doi.org/10.1038/372475a0>.
 22. Bösl, B., Grimminger, V., and Walter, S. (2006). The molecular chaperone Hsp104—A molecular machine for protein disaggregation. *J. Struct. Biol.* 156, 139–148. <https://doi.org/10.1016/j.jsb.2006.02.004>.
 23. Sweeny, E.A., and Shorter, J. (2016). Mechanistic and Structural Insights into the Prion-Disaggregation Activity of Hsp104. *J. Mol. Biol.* 428, 1870–1885. <https://doi.org/10.1016/j.jmb.2015.11.016>.
 24. Tessarz, P., Mogk, A., and Bukau, B. (2008). Substrate threading through the central pore of the Hsp104 chaperone as a common mechanism for protein disaggregation and prion propagation. *Mol. Microbiol.* 68, 87–97. <https://doi.org/10.1111/j.1365-2958.2008.06135.x>.
 25. Jackrel, M.E., DeSantis, M.E., Martinez, B.A., Castellano, L.M., Stewart, R.M., Caldwell, K.A., Caldwell, G.A., and Shorter, J. (2014). Potentiated Hsp104 Variants Antagonize Diverse Proteotoxic Misfolding Events. *Cell* 156, 170–182. <https://doi.org/10.1016/j.cell.2013.11.047>.
 26. Torrente, M.P., Chuang, E., Noll, M.M., Jackrel, M.E., Go, M.S., and Shorter, J. (2016). Mechanistic Insights into Hsp104 Potentiation. *J. Biol. Chem.* 291, 5101–5115. <https://doi.org/10.1074/jbc.M115.707976>.
 27. Tariq, A., Lin, J., Noll, M.M., Torrente, M.P., Mack, K.L., Murillo, O.H., Jackrel, M.E., and Shorter, J. (2018). Potentiating Hsp104 activity via phosphomimetic mutations in the middle domain. *FEMS Yeast Res.* 18, foy042. <https://doi.org/10.1093/femsyr/foy042>.
 28. Rampelt, H., Kirstein-Miles, J., Nillegoda, N.B., Chi, K., Scholz, S.R., Morimoto, R.I., and Bukau, B. (2012). Metazoan Hsp70 machines use Hsp110 to power protein disaggregation: Disaggregation by animal Hsp110-Hsp70-Hsp40. *EMBO J.* 31, 4221–4235. <https://doi.org/10.1038/emboj.2012.264>.
 29. Mattoo, R.U.H., Sharma, S.K., Priya, S., Finka, A., and Goloubinoff, P. (2013). Hsp110 Is a Bona Fide Chaperone Using ATP to Unfold Stable Misfolded Polypeptides and Reciprocally Collaborate with Hsp70 to Solubilize Protein Aggregates. *J. Biol. Chem.* 288, 21399–21411. <https://doi.org/10.1074/jbc.M113.479253>.
 30. Finka, A., Sharma, S.K., and Goloubinoff, P. (2015). Multi-layered molecular mechanisms of polypeptide holding, unfolding and disaggregation by HSP70/HSP110 chaperones. *Front. Mol. Biosci.* 2, 29. <https://doi.org/10.3389/fmolb.2015.00029>.
 31. Gao, X., Carroni, M., Nussbaum-Krammer, C., Mogk, A., Nillegoda, N.B., Szlachcic, A., Guilbride, D.L., Saibil, H.R., Mayer, M.P., and Bukau, B. (2015). Human Hsp70 Disaggregase Reverses Parkinson's-Linked α -Synuclein Amyloid Fibrils. *Mol. Cell* 59, 781–793. <https://doi.org/10.1016/j.molcel.2015.07.012>.
 32. Nillegoda, N.B., Kirstein, J., Szlachcic, A., Berynsky, M., Stank, A., Stengel, F., Arnsburg, K., Gao, X., Scior, A., Aebersold, R., et al. (2015). Crucial HSP70 co-chaperone complex unlocks metazoan protein disaggregation. *Nature* 524, 247–251. <https://doi.org/10.1038/nature14884>.
 33. Gonçalves, C.C., Sharon, I., Schmeing, T.M., Ramos, C.H.I., and Young, J.C. (2021). The chaperone HSPB1 prepares protein aggregates for resububilization by HSP70. *Sci. Rep.* 11, 17139. <https://doi.org/10.1038/s41598-021-96518-x>.
 34. Gupta, R., Kasturi, P., Bracher, A., Loew, C., Zheng, M., Vilella, A., Garza, D., Hartl, F.U., and Raychaudhuri, S. (2011). Firefly luciferase mutants as sensors of proteome stress. *Nat. Methods* 8, 879–884. <https://doi.org/10.1038/nmeth.1697>.
 35. Zhou, C., Slaughter, B.D., Unruh, J.R., Eldakak, A., Rubinstein, B., and Li, R. (2011). Motility and Segregation of Hsp104-Associated Protein Aggregates in Budding Yeast. *Cell* 147, 1186–1196. <https://doi.org/10.1016/j.cell.2011.11.002>.
 36. Escusa-Toret, S., Vonk, W.I.M., and Frydman, J. (2013). Spatial sequestration of misfolded proteins by a dynamic chaperone pathway enhances cellular fitness during stress. *Nat. Cell Biol.* 15, 1231–1243. <https://doi.org/10.1038/ncb2838>.
 37. Zhang, M., Chang, H., Zhang, Y., Yu, J., Wu, L., Ji, W., Chen, J., Liu, B., Lu, J., Liu, Y., et al. (2012). Rational design of true monomeric and bright photoactivatable fluorescent proteins. *Nat. Methods* 9, 727–729. <https://doi.org/10.1038/nmeth.2021>.
 38. Zhou, C., Slaughter, B.D., Unruh, J.R., Guo, F., Yu, Z., Mickey, K., Narkar, A., Ross, R.T., McClain, M., and Li, R. (2014). Organelle-Based Aggregation and Retention of Damaged Proteins in Asymmetrically Dividing Cells. *Cell* 159, 530–542. <https://doi.org/10.1016/j.cell.2014.09.026>.
 39. Wu, G.-H., Mitchell, P.G., Galaz-Montoya, J.G., Hecksel, C.W., Sontag, E.M., Gangadharan, V., Marshman, J., Mankus, D., Bisher, M.E., Lytton-Jean, A.K.R., et al. (2020). Multi-scale 3D Cryo-Correlative Microscopy for Vitri-fied Cells. *Structure* 28, 1231–1237.e3. <https://doi.org/10.1016/j.str.2020.07.017>.
 40. Ruan, L., Zhou, C., Jin, E., Kucharavy, A., Zhang, Y., Wen, Z., Florens, L., and Li, R. (2017). Cytosolic proteostasis through importing of misfolded proteins into mitochondria. *Nature* 543, 443–446. <https://doi.org/10.1038/nature21695>.
 41. Larimer, F.W., and Stevens, A. (1990). Disruption of the gene XRN1, coding for a 5' → 3' exoribonuclease, restricts yeast cell growth. *Gene* 95, 85–90. [https://doi.org/10.1016/0378-1119\(90\)90417-P](https://doi.org/10.1016/0378-1119(90)90417-P).
 42. Becker, J., Walter, W., Yan, W., and Craig, E.A. (1996). Functional Interaction of Cytosolic hsp70 and a DnaJ-Related Protein, Ydj1p, in Protein Translocation In Vivo. *Mol. Cell Biol.* 16, 4378–4386. <https://doi.org/10.1128/MCB.16.8.4378>.
 43. Shaner, L., Sousa, R., and Morano, K.A. (2006). Characterization of Hsp70 Binding and Nucleotide Exchange by the Yeast Hsp110 Chaperone Sse1. *Biochemistry* 45, 15075–15084. <https://doi.org/10.1021/bi061279k>.
 44. Heinisch, J. (1986). Isolation and characterization of the two structural genes coding for phosphofructokinase in yeast. *Mol. Gen. Genet.* 202, 75–82. <https://doi.org/10.1007/BF00330520>.
 45. Peñalosa-Ruiz, G., Aranda, C., Ongay-Larios, L., Colon, M., Quezada, H., and Gonzalez, A. (2012). Paralogous ALT1 and ALT2 Retention and Diversification Have Generated Catalytically Active and Inactive Aminotransferases in Saccharomyces cerevisiae. *PLoS One* 7, e45702. <https://doi.org/10.1371/journal.pone.0045702>.
 46. Costa, E.A., Subramanian, K., Nunnari, J., and Weissman, J.S. (2018). Defining the physiological role of SRP in protein-targeting efficiency and specificity. *Science* 359, 689–692. <https://doi.org/10.1126/science.aar3607>.
 47. Bukau, B., and Horwich, A.L. (1998). The Hsp70 and Hsp60 Chaperone Machines. *Cell* 92, 351–366. [https://doi.org/10.1016/S0092-8674\(00\)80928-9](https://doi.org/10.1016/S0092-8674(00)80928-9).
 48. Mayer, M.P., and Bukau, B. (2005). Hsp70 chaperones: Cellular functions and molecular mechanism. *Cell. Mol. Life Sci.* 62, 670–684. <https://doi.org/10.1007/s00018-004-4464-6>.
 49. Kampinga, H.H., and Craig, E.A. (2010). The HSP70 chaperone machinery: J proteins as drivers of functional specificity. *Nat. Rev. Mol. Cell Biol.* 11, 579–592. <https://doi.org/10.1038/nrm2941>.
 50. Eaglestone, S.S., Ruddock, L.W., Cox, B.S., and Tuite, M.F. (2000). Guanidine hydrochloride blocks a critical step in the propagation of the prion-like determinant [PSI⁺] of *Saccharomyces cerevisiae*. *Proc. Natl. Acad. Sci. USA* 97, 240–244. <https://doi.org/10.1073/pnas.97.1.240>.
 51. Jung, G., and Masison, D.C. (2001). Guanidine Hydrochloride Inhibits Hsp104

- Activity In Vivo: A Possible Explanation for Its Effect in Curing Yeast Prions. *Curr. Microbiol.* 43, 7–10. <https://doi.org/10.1007/s002840010251>.
52. Jung, G., Jones, G., and Masison, D.C. (2002). Amino acid residue 184 of yeast Hsp104 chaperone is critical for prion-curing by guanidine, prion propagation, and thermotolerance. *Proc. Natl. Acad. Sci. USA* 99, 9936–9941. <https://doi.org/10.1073/pnas.152333299>.
 53. Kummer, E., Oguchi, Y., Seyffer, F., Bukau, B., and Mogk, A. (2013). Mechanism of Hsp104/ClpB inhibition by prion curing Guanidinium hydrochloride. *FEBS Lett.* 587, 810–817. <https://doi.org/10.1016/j.febslet.2013.02.011>.
 54. Kato, M., Han, T.W., Xie, S., Shi, K., Du, X., Wu, L.C., Mirzaei, H., Goldsmith, E.J., Longgood, J., Pei, J., et al. (2012). Cell-free Formation of RNA Granules: Low Complexity Sequence Domains Form Dynamic Fibers within Hydrogels. *Cell* 149, 753–767. <https://doi.org/10.1016/j.cell.2012.04.017>.
 55. Doyle, S.M., and Wickner, S. (2009). Hsp104 and ClpB: protein disaggregating machines. *Trends Biochem. Sci.* 34, 40–48. <https://doi.org/10.1016/j.tibs.2008.09.010>.
 56. Yu, H., Lu, S., Gasior, K., Singh, D., Vazquez-Sanchez, S., Tapia, O., Toprani, D., Beccari, M.S., Yates, J.R., Da Cruz, S., et al. (2021). HSP70 chaperones RNA-free TDP-43 into anisotropic intranuclear liquid spherical shells. *Science* 371, eabb4309. <https://doi.org/10.1126/science.abb4309>.
 57. Kaimal, J.M., Kandasamy, G., Gasser, F., and Andréasson, C. (2017). Coordinated Hsp110 and Hsp104 Activities Power Protein Disaggregation in *Saccharomyces cerevisiae*. *Mol. Cell Biol.* 37, e00027–17. <https://doi.org/10.1128/MCB.00027-17>.
 58. Wentink, A.S., Nillegoda, N.B., Feufel, J., Ubartaitė, G., Schneider, C.P., De Los Rios, P., Hennig, J., Barducci, A., and Bukau, B. (2020). Molecular dissection of amyloid disaggregation by human HSP70. *Nature* 587, 483–488. <https://doi.org/10.1038/s41586-020-2904-6>.
 59. Eichler, C.E., Hakes, A.C., Hull, B., and Gavis, E.R. (2020). Compartmentalized oskar degradation in the germ plasm safeguards germline development. *Elife* 9, e49988. <https://doi.org/10.7554/eLife.49988>.
 60. Sathyanarayanan, U., Musa, M., Bou Dib, P., Raimundo, N., Milosevic, I., and Krisko, A. (2020). ATP hydrolysis by yeast Hsp104 determines protein aggregate dissolution and size in vivo. *Nat. Commun.* 11, 5226. <https://doi.org/10.1038/s41467-020-19104-1>.
 61. Patel, A., Malinowska, L., Saha, S., Wang, J., Alberti, S., Krishnan, Y., and Hyman, A.A. (2017). ATP as a biological hydrotrope. *Science* 356, 753–756. <https://doi.org/10.1126/science.aaf6846>.
 62. Longtine, M.S., McKenzie, A., Iij, Demarini, D.J., Shah, N.G., Wach, A., Brachat, A., Philippsen, P., and Pringle, J.R. (1998). Additional modules for versatile and economical PCR-based gene deletion and modification in *Saccharomyces cerevisiae*. *Yeast* 14, 953–961. [https://doi.org/10.1002/\(SICI\)1097-0061\(199807\)14:10<953::AID-YEA293>3.0.CO;2-U](https://doi.org/10.1002/(SICI)1097-0061(199807)14:10<953::AID-YEA293>3.0.CO;2-U).

STAR★METHODS

KEY RESOURCES TABLE

REAGENT or RESOURCE	SOURCE	IDENTIFIER
Antibodies		
Pgk1 mouse monoclonal antibody	Invitrogen	Cat #: 459250; RRID:AB_2532235 lot UK2878625A
GFP Living Colors A.v. mAb clone JL-8	Takara Bio	Cat #: 632381; RRID:AB_10013427 lot 5
IRDye 800CW Goat anti-Mouse	LI-COR	Cat #: 926-32210; RRID:AB_621842 lot C91210-09
IRDye 680RD Goat anti-Rabbit	LI-COR	Cat #: 926-68071; RRID:AB_10956166 lot D11012-15
Bacterial and virus strains		
NEB 5-alpha Competent <i>E. coli</i> (High Efficiency)	NEB	Cat #: C2987
Chemicals, peptides, and recombinant proteins		
β -estradiol	Sigma-Aldrich	Cat #: E2758-1G
Guanidine hydrochloride (GdnHCl)	Invitrogen	Cat #: 15502-016
Concavalin (ConA)	Sigma	Cat #: L7647
G418	Corning	Cat #: 61-234-RG
Critical commercial assays		
1x Bolt™ LDS sample buffer	Invitrogen	Cat #: B0008
10-well 4-12% NuPAGE Bis-Tris gel	Invitrogen	Cat #: NW04122BOX
Precision Plus Protein™ Dual Color Standard	Bio-Rad	Cat #: 1610374
iBlot™ 2 Transfer Stacks, PVDF, mini	Invitrogen	Cat #: IB24002
Odyssey Blocking Buffer	LI-COR	Cat #: 927-40000
Bovine serum albumin (BSA)	Sigma	Cat #: A9647
Frozen-EZ Yeast Transformation II Kit	Zymo Research	Cat #: T2001
Gibson Assembly Master Mix	NEB	Cat #:M5510A, lot 10056329
Experimental models: Organisms/strains		
MATa his3 Δ 1; leu2 Δ 0; met15 Δ 0; ura3 Δ 0	N/A	RLY10351
<i>trp::pTDH-FlucSM-GFP-3xFLAG-KanMX</i>	Ruan, L. et al., 2017. ⁴⁰	RLY8595
Δ <i>hsp104::KanMX</i> ; <i>amp::FlucSM-GFP-3xFLAG-3xFKBP-HIS3</i> ; <i>trp::MTS-mCherry-GFP1-10-NatMX</i>	Ruan, L. et al., 2017. ⁴⁰	RLY8653
<i>trp::pTDH-FlucSM-GFP-3xFLAG-URA3</i>	This manuscript	RLY10354
<i>trp::pTDH-FlucSM-mEos3.2-3xFLAG-KanMX</i>	This manuscript	RLY10355
<i>ALD6-RFP-HPH trp::pTDH-FlucSM-GFP-3xFLAG-KanMX</i>	This manuscript	RLY10356
<i>CDC19-GFP-HIS trp::pTDH-FlucSM-mCherry-3xFLAG-KanMX</i>	This manuscript	RLY10357
<i>SUP45-GFP-HIS trp::pTDH-FlucSM-mCherry-3xFLAG-KanMX</i>	This manuscript	RLY10358
<i>ALD6-GFP-HIS</i>	GFP library	RLY10359
<i>trp::pTDH-FlucSM-GFP-3xFLAG-URA3</i> ; <i>trp::MTS-mCherry-NatMX</i>	This manuscript	RLY10360
Δ <i>hsp104::KanMX</i> ; <i>trp::pTDH-FlucSM-GFP-3xFLAG-URA3</i> ; <i>trp::MTS-mCherry-NatMX</i>	This manuscript	RLY10361
Δ <i>pfk1::KanMX</i> ; <i>trp::pTDH-FlucSM-GFP-3xFLAG-URA3</i> ; <i>trp::MTS-mCherry-NatMX</i>	This manuscript	RLY10362
Δ <i>xm1::KanMX</i> ; <i>trp::pTDH-FlucSM-GFP-3xFLAG-URA3</i> ; <i>trp::MTS-mCherry-NatMX</i>	This manuscript	RLY10363

(Continued on next page)

Continued

REAGENT or RESOURCE	SOURCE	IDENTIFIER
Δ sse1::KanMX; trp::pTDH-FlucSM-GFP-3xFLAG-URA3; trp::MTS-mCherry-NatMX	This manuscript	RLY10364
Δ new1::KanMX; trp::pTDH-FlucSM-GFP-3xFLAG-URA3; trp::MTS-mCherry-NatMX	This manuscript	RLY10365
Δ aro4::KanMX; trp::pTDH-FlucSM-GFP-3xFLAG-URA3; trp::MTS-mCherry-NatMX	This manuscript	RLY10366
Δ alt2::KanMX; trp::pTDH-FlucSM-GFP-3xFLAG-URA3; trp::MTS-mCherry-NatMX	This manuscript	RLY10367
Δ his4::KanMX; trp::pTDH-FlucSM-GFP-3xFLAG-URA3; trp::MTS-mCherry-NatMX	This manuscript	RLY10368
Oligonucleotides		
Hsp104 genotyping GAG GAA GCT GAA GAA TGT CTG G	This manuscript	AT36
Hsp104 genotyping CTT TTG CTC GGG TGT CAA GTT C	This manuscript	AT37
Create FlucSM-GFP::URA3 plasmid gctggagctcTTCAATTCATCA TTTTTTTTTATTCTTTTTTTGATTC	This manuscript	AT273:
Create FlucSM-GFP::URA3 plasmid atgaattgaaGAGCTCCAGCT TTTGTTCC	This manuscript	AT274
Create FlucSM-GFP::URA3 plasmid gcaaaactaaGAGCTCAGTTT ATCATTATCAATAC	This manuscript	AT218
Create FlucSM-GFP::URA3 plasmid aactgagctcTTAGTTTTGCTG GCCGCATC	This manuscript	AT221
Create FlucSM-mEos3.2::KAN plasmid tgccagacgaGAATTCGAT ATCAAGCTTATCGATACCGCAGGTGGC	This manuscript	AT214
Create FlucSM-mEos3.2::KAN plasmid tcgcactcatGGTGCCGAC CGGCCGGTG	This manuscript	AT215
Create FlucSM-mEos3.2::KAN plasmid ggctgccaccATGAGTGCG ATTAAGCCAG	This manuscript	AT216
Create FlucSM-mEos3.2::KAN plasmid tatcgaattcTCGTCTGGCA TTGTCAGG	This manuscript	AT217
Confirm GFP and mEos sequence GGA AAA AGA GAT CGT GGA TTA CG	This manuscript	AT242
Integrate Hsp104 variants into genome AACAAAGAAAAAGAA ATCAACTACACGTACCATAAAAATACAGAATAT ATGAACGA CCAAACGCAATTTAC	This manuscript	AT521
Integrate Hsp104 variants into genome TAT ATT ACT GAT TCT TGT TCG AAA GTT TTT AAA AAT CAC ACT ATA TTA AA GAG CAG ATT GTA CTG AGA GTG C	This manuscript	AT522
Hsp104 sequencing CTG TAG GTA AGG GAC TGA TCC	This manuscript	AT443
Hsp104 sequencing ATGAACGACCAACGCAATTTAC	This manuscript	AT444
Hsp104 sequencing GAC GTT CCC ACT ATC TTA CAA GG	This manuscript	AT445
Hsp104 sequencing GCTGAACGTAGATATGATACTGC	This manuscript	AT446
Hsp104 sequencing GCTGTTAGGCAACATTTACAGAC	This manuscript	AT447

(Continued on next page)

Continued

REAGENT or RESOURCE	SOURCE	IDENTIFIER
Create hsp104 overexpression plasmid tatactttaacgtcaaggagAT GAACGACCAAACGCAATTTAC	This manuscript	AT440
Create hsp104 overexpression plasmid attcgctatttagaagtgTTA ATCTAGGTCATCATCAATTTCC	This manuscript	AT441
Ald6-GFP test primers CAGAATCTTTGAGCACAGGTTTG	This manuscript	AT478
Ald6-GFP test primers CGT ATT GTC CCT GAT CCA TAC C	This manuscript	AT479
Sup45-GFP test primers GGT ATT GGT GCC ATG CTG C	This manuscript	AT482
Sup45-GFP test primers CAA GTG ATG TTG CTG CTA GAG G	This manuscript	AT483
Cdc19-GFP test primers CAG ATG CCC AAG AGC TGC TA	This manuscript	AT486
Cdc19-GFP test primers CAG AAG CTG AAC ATA GTT CAC TGG	This manuscript	AT487
Xrn1 KO test primers CAAATATAACAGTTGCAGCTTGC	This manuscript	AT246
Xrn1 KO test primers GAG AAC AGG TTT GCC ATT ATG C	This manuscript	AT248
Pfk1 KO test primers CGT CTA CTC AAG TCT CGC C	This manuscript	AT390
Pfk1 KO test primers CGC AGA TTA AGC ACA CCC	This manuscript	AT391
Sse1 KO test primers GAAGCCACATGAATTGAGAAAGGTAAGC	This manuscript	AT525
Sse1 KO test primers GAA TCA GAT GCT GAT GAA GGC TGG	This manuscript	AT526
New1 KO test primers CGAAAGATACAACAGAGCCATGTG	This manuscript	AT540
New1 KO test primers CAC TCC CTA GTA CAA CCT CTT ACC	This manuscript	AT541
Aro4 KO test primers GGACGCATTGTTAGCTCATTGAATAC	This manuscript	AT528
Aro4 KO test primers CTG CTA CTT CAA TAG CTG CCT C	This manuscript	AT529
Alt2 KO test primers GAGGCTTCTCCTACTTGTGG	This manuscript	AT537
Alt2 KO test primers GAA AGG AGG AGT CAC CAT AGG TG	This manuscript	AT538
His4 KO test primers GAGCATTGCGATACGATGGGTC	This manuscript	AT546
His4 KO test primers CCA CTA TAA ACC CGT TCT TCA TGG C	This manuscript	AT547
Glk1 KO test primers CCTATCTTGGGCGTGGTGTC	This manuscript	AT543
Glk1 KO test primers GTA ACT GGT TAG CGG CGG AG	This manuscript	AT544
Recombinant DNA		
pJW1663	Addgene	Plasmid #112037
RLB1140	GapP-FlucSM-GFP-FLAG Trp1p-TRP1-KAN	Ruan, L. et al., 2017 ⁴⁰

(Continued on next page)

Continued

REAGENT or RESOURCE	SOURCE	IDENTIFIER
RLB1141	GapP-FlucSM-GFP-FLAG Trp1p-TRP1 Ura3p-URA3	This manuscript
RLB1142	GapP-FlucSM-mEos3.2-FLAG Trp1p-Trp1-KAN	This manuscript
RLB1143	pJW1663-Hsp104	This manuscript

Software and algorithms

ImageJ	NIH	https://imagej.nih.gov/ij/
MetaMorph Version 7.0	MDS Analytical Technologies	N/A
Carl Zeiss ZEN	Carl Zeiss	https://www.zeiss.com/
Imaris Version 9.8.1	Oxford Instruments	
Graphpad Prism Version 9.4.1	Graphpad Prism	https://www.graphpad.com/
Image Studio (LI-COR) software	LI-COR	http://licor.com

Other

Yokogawa CSU-10 spinning disc on the side port of a Carl Zeiss 200-m inverted confocal microscope (100x oil immersion lens, 1.45 NA objective)	Carl Zeiss	N/A
Zeiss LSM880 confocal (63x oil objective, 1.4 NA objective)	Carl Zeiss	N/A
VWR Vistavision microscope slides, Plain, 3 x 1", 1 mm thick	VWR	Cat # 16004-430 LOT 42533
VWR micro cover glass, 22x22mm No. 1.5	VWR	Cat # 48366-227, lot 21829
MatTek 35 mm glassbottom culture dish	MatTek	Cat #: P35G-1.5-14-C, lot TKO-P351173-409
TetraSpeck 0.1 μM diameter fluorescent beads	TetraSpeck™	Cat #: T7279
iBlot 2 system	Thermo	N/A
LI-COR Odyssey® Fc Imaging system	LI-COR	N/A

Deposited data

AggregateDissolution_macro.ijm	³⁵	Mendeley Data, V1, https://doi.org/10.17632/n666jb2zhp.1
CSV files to generate figures	This manuscript	Mendeley Data, V1, https://doi.org/10.17632/n666jb2zhp.1
Raw immunoblot files	This manuscript	Mendeley Data, V1, https://doi.org/10.17632/n666jb2zhp.1

RESOURCE AVAILABILITY**Lead contact**

Further information and requests for resources and reagents should be directed to and will be fulfilled by the corresponding authors, Rong Li (rong@jhu.edu) or Jian Liu (jliu187@jhmi.edu).

Materials availability

All strains and plasmids generated in this study are available upon request from the corresponding author.

Data and code availability

- All data needed to evaluate the conclusions are available in the manuscript. All files that were used to generate the figures in the manuscript and raw immunoblot files have been deposited to the Mendeley Data general-purpose repository and can be found here: tomaszewski, alexis (2023), "Solid-to-Liquid Phase Transition in the Dissolution of Cytosolic Misfolded-Protein Aggregates", Mendeley Data, V1, <https://doi.org/10.17632/n666jb2zhp.1>.
- This study utilized previously published code to calculate the average aggregate intensity over time for dissolution analysis and the ImageJ macro is available in Mendeley Data as AggregateDissolution_macro.ijm.³⁵

- Any additional information required to reanalyze the data reported in this paper is available from the [lead contact](#) upon request, such as the raw imaging datasets that have not been deposited in a public repository because of the large size of the imaging files and screening data.

EXPERIMENTAL MODEL AND STUDY PARTICIPANT DETAILS

Yeast *saccharomyces cerevisiae*

Yeast strains used in this study are based on the BY4741 strain background. Gene deletions and GFP tagging were performed with PCR mediated homologous combination and the integration was confirmed through PCR.⁶² Photoconvertible FlucSM-mEos3.2 was created by replacing the GFP in the FlucSM-GFP plasmid with the mEos3.2 fluorophore.³⁷

To generate the strains for the aggregate subset screen, a plasmid encoding FlucSM-GFP was transformed into the KO strains that had the mitochondria labeled with MTS-mCherry-GFP₁₋₁₀ with the Frozen-EZ Yeast Transformation II Kit following the microscale protocol in 96-well format (T2001, Zymo Research). Knockout strains with MTS-mCherry-GFP₁₋₁₀ were grown in deep-well plates containing 1 ml of YPD media with G418 (200 µg/mL, Corning, Cat #: 61-234-RG). The transformation was carried out with the epMotion 5075 liquid handling workstation (Eppendorf) and 150 µL of refreshed logarithmic phase cultures plus 0.2 µg of Bsu36I (NEB, Cat #: R0524S) linearized FlucSM-GFP-URA3 DNA were added to the Frozen-EZ Yeast solution mix. The transformation mixtures were incubated for 2 hours at 30°C. Following incubation, they were transferred into deep-well plates with 4 volumes of SD-Ura media with shaking at 250 rpm at 30°C for outgrowth for 5 days.

To create a plasmid to induce expression of Hsp104, *HSP104* gene was cloned into a plasmid containing the β-estradiol-inducible system (from pJW1663, Addgene plasmid #112037). pJW1663 was digested with EcoRI and AclI, replacing the GFP sequence with Hsp104, and then stably integrated into yeast genome.⁴⁶ The *hsp104* variant plasmids were kindly provided by J. Shorter's laboratory. The variant genes were amplified through PCR and integrated into yeast genome to replace the Δ*hsp104*::KANMX allele at the endogenous *HSP104* gene in strains expressing FlucSM-GFP.

Yeast cells were grown in synthetic complete (SC) medium and cultured overnight at 30°C (23°C for temperature-sensitive mutants). The overnight cultures were diluted into a 5 ml culture, grown for 4 hours to reach a logarithmic phase with an optical density (OD₆₀₀) of roughly 0.5, and transferred to 42°C shaker to be heat shocked for 30 min with rotation. Following heat shock, cells were recovered at 30°C.

METHOD DETAILS

Microscopy

Live-cell images of yeast were acquired on a Yokogawa CSU-10 spinning disc on the side port of a Carl Zeiss 200-m inverted confocal microscope (100x oil immersion lens, 1.45 numerical aperture (NA) PlanApoChromat objective, 13-15 0.5 µm Z-slices covering a 6.5 to 7.5 µm range) and FLIP and photoconversion assays were performed using a Zeiss LSM880 confocal (63x oil objective, 1.4 NA PlanApoChromat objective, single slices). Images were acquired using MetaMorph (version 7.0; MDS Analytical Technologies) on a CSU-10 spinning disc system and Carl Zeiss ZEN software on the LSM880. The 448 nm and 561 nm excitation lasers were used to excite GFP or mCherry respectively, and the emission was collected through the appropriate filters onto a Hamamatsu C9100-13 EMCCD on the spinning disc confocal system.

Yeast cells were grown in synthetic complete (SC) medium and cultured overnight at 30°C (23°C for temperature-sensitive mutants). The overnight cultures were diluted into a 5 ml culture, grown for 4 hours to reach a logarithmic phase with an optical density (OD₆₀₀) of roughly 0.5, and transferred to 42°C shaker to be heat shocked for 30 min at 160 rpm. For single time point imaging, 1 ml of the refreshed culture was concentrated through centrifugation to ~10 µl and 1 µl was applied to a microscope slide. For 3D fluorescence time-lapse imaging, 1 ml of the refreshed mid-log culture was concentrated through centrifugation to ~100 µl and applied to a Concavalin (ConA) coated 35-mm glass-bottomed dish for 5 min to immobilize the yeast. Cells were washed with SC media and fresh SC medium was added (or SC with drugs where indicated) prior to imaging. 3D image stacks with 15 0.5 µm steps were acquired every minute for 90-150 min. Image processing was performed using Image J (NIH) or Imaris software. All representative images in this paper were displayed as maximum intensity projections.

Aggregate dissolution assays

Aggregates were induced with a 30 min heat shock at 42°C with shaking. Cells were recovered for 10 min at 30°C or 23°C (for temperature sensitive mutants), adhered to a ConA coated 35-mm glass-bottomed dish for 5 min to immobilize the yeast, and washed in fresh media prior to imaging at room temperature. Since aggregates recovered for 10 min with rotating and 5 min on a dish, the 0 time point of movies is roughly 15 min with recovery.

Aggregate dissolution assays were performed on a Yokogawa CSU-10 spinning disc on the side port of a Carl Zeiss 200-m inverted confocal microscope described above. FlucSM-GFP labeled aggregates were imaged with a 200 ms exposure and 6% laser power, 13-15 0.5 µm Z-slices covering a 6.5 to 7.5 µm range, for 1 minute intervals until aggregates dissolved (90 – 150 min). The pixel size was 0.144578 µm/pixel.

All images were processed as follows. First, a maximum intensity projection was made using the Z stack images. Secondly, the background was subtracted using ImageJ and a rolling ball radius of 50.0 pixels. Aggregate dissolution assays were quantified as described previously.³⁵ Briefly, to calculate the average aggregate intensity, first a mask of the cell, a mask of the aggregates, and the cytoplasm (excluding aggregates) was generated. Then we could generate the average aggregate area, average intensity, and average cell intensity excluding the aggregates. The average intensity in the cytoplasm was subtracted from the average aggregate region intensity and multiplied by the average

aggregate area for each time point to generate the average aggregate intensity. This was normalized to the average aggregate intensity at the first three time points for comparisons between strains and conditions. Image intensities have been scaled so that the cell background can be seen as a reference for where the cells were relative to the protein aggregates for visualization purposes. Because some strains have higher aggregate intensities than others, some images may appear saturated but the fluorescence intensity of the images is well below the range of saturation and imaged uniformly amongst strains and conditions.

To calculate the average aggregate number per cell, the maximum intensity projection was background subtracted and then smoothed in ImageJ and local maxima were used to detect the number of spots in a field. The number of cells were counted, and the number of spots were divided by the number of cells to obtain the average aggregate number per cell at 10 to 30 min intervals for movies. To calculate the half-time of aggregate dissolution, the time in which aggregates decreased to 50 % was indicated for both intensity and number for 3 movies.

Aggregate subset screen

Yeast KO strains with deletion of genes encoding aggregate enriched proteins were grown and prepared similarly to aggregate dissolution assays, except aggregates were imaged at single time points before HS, immediately after a 30 min HS (0 min) at 42°C, and after a 30 min recovery at 30°C (30 min). Imaging was performed on a Yokogawa CSU-10 spinning disc on the side port of a Carl Zeiss 200-m inverted confocal microscope described above. FlucSM-GFP labeled aggregates were imaged with a 200 ms exposure and 6% laser power, 13 0.5 μm Z-slices covering a 6.5 μm range, for single time point images. The pixel size was 0.144578 $\mu\text{m}/\text{pixel}$. Three fields were acquired for each strain at each time point. Aggregate number at 0 and 30 min was calculated for each strain and compared to WT. The strains with a significantly greater number of aggregates at after HS that persisted into 30 min recovery were selected for further validation and detailed characterization.

FLIP experiments

For FLIP assays, cells were prepared on either slides or on ConA coated dishes (for drug treatments experiments) and a single image was acquired for each time point. FLIP assays were performed using a Zeiss LSM880 confocal described above. FlucSM-GFP labeled aggregates were imaged with 1% laser power with a 63x oil objective with 15x zoom resulting in a 9 x 9 μm imaging region. The pinhole was set to 565 μm and the pixel dwell time was 0.24 μs . Two frames were acquired before photobleaching, and then half of an aggregate was continuously bleached with a laser power of 30% for the duration of the 44 sec movie for 100 time points. The pixel size was 0.017581 $\mu\text{m}/\text{pixel}$.

To quantify the intensity over time, the mean intensity was calculated for the bleached region and non-bleached region and corrected for photobleaching by subtracting the mean cytoplasmic intensity for each time point. Non-bleached aggregates were quantified in the same cell or neighboring cells in the same field as photobleached aggregates. To estimate exponential decay rates, the curves were fit to $y=y_0e^{-kt}$. Since we normalized all FLIP curves to the initial intensity at the start of the movie, y_0 was set to 1. All negative values for corrected region of interests were omitted for exponential fitting analysis when the bleached regions showed a similar intensity to the cell background. The half-life was determined by the formula $t_{1/2}=\ln(2)/k$. The immobile fraction was calculated by comparing the mean intensity of the curves at the end of the movies and the value at this last time point was used for statistical analysis.

Photoconversion

For mEos3.2 photoconversion assays, cells were prepared on ConA coated dishes after HS on a Zeiss LSM880 confocal described above (63x oil objective) with 5x zoom resulting in a 26.99 x 26.99 μm imaging region. The pinhole was set to 55 μm and the pixel dwell time was 0.38 μs . 2 images were acquired prior to photoconversion with both the 488 nm and 561 laser with a laser power of 1% each at a single focal plane. Then, the 405 nm laser was used to convert an entire aggregate for 8 iterations at a single z slice. Following photoconversion, 3D image stacks with 7 0.5 μm steps were acquired every two minutes using both 488 nm and 561 nm excitation lasers (1% laser power) until dissolution was complete. The pixel size was 0.052715 $\mu\text{m}/\text{pixel}$.

We performed deconvolution analysis on the FluSM-mEos3.2 photoconversion experiments using TetraSpeck T72790.1 μm diameter fluorescent beads that allowed us to determine the point spread functions for the LSM880 confocal microscope through the Deconvolution 2 plugin in ImageJ. We quantified the aggregate intensity for the photoconverted aggregate relative to the original aggregate it merged with. First, we created a mask of the photoconverted aggregate ROI over time. Next, we quantified the aggregate intensity in both channels for each ROI. Then we normalized the intensity to $t = 44$ min for quantification.

Circularity

To measure aggregate circularity, a mask was made of the aggregates and circularity was measured with the formula $4\pi \cdot (\text{area}/\text{perimeter}^2)$ and compared at 15 min time intervals during dissolution. Aggregates with an area less than 10 pixels were omitted for analysis because they were too small for their shape to be resolved.

Lineage tracing

To track the fate of individual aggregates during dissolution, we used Imaris 9.8.1 software to detect and track aggregates. First we used spot detection to identify aggregates in a single cell. Then we used the tracking feature and set the max gap to 2 frames. We connected or

disconnected objects to amend the results of the automated tracking technology. From there we were able to generate a lineage tree with branches to depict clustering and fusion events. For cells with >10 aggregates, we showed only a subset of the tracks for visualization purposes. We then statistically coded the aggregate tracks by the mean intensity of the aggregate for each track.

Immunoblot analysis

Yeast overnight cultures were diluted into a 5ml culture and grown 4 hours to reach a logarithmic phase with an OD that was roughly 0.5 and transferred to 42°C shaker to be heat shocked for 30 min. Samples were pelleted, washed with 1 ml of H₂O, and snap frozen in liquid nitrogen. Samples were resuspended in 50 μL of autoclaved H₂O. 150 μL of 0.2N NaOH and 10 μL of beta-mercaptoethanol (BME) were added. The samples were incubated on ice for 10 minutes and then vortexed at top speed at 4°C. the supernatant was discarded and the pellet was re-suspended in 200 μL 1x Bolt™ LDS sample buffer (Invitrogen, Cat #: B0008) supplemented with 10% BME. Samples were boiled for 15 minutes, centrifuged, and then vortexed prior to loading 15 μL of each sample onto a 10-well 4-12% NuPAGE Bis-Tris gel (Invitrogen, Cat #: NW04122BOX) along with 10 μL Precision Plus Protein™ Dual Color Standard (Bio-Rad, Cat #: 1610374). SDS-PAGE gels were run according to manufacturer's recommendation.

The gel was next transferred to a PVDF membrane (Invitrogen, Cat #: IB24002) using the iBlot™ 2 transfer system. Membranes were blocked in Odyssey Blocking Buffer (PBS) (LI-COR, Cat #: 927-40000) for 1 hour at room temperature followed by overnight incubation in primary antibody in 5% bovine serum albumin (BSA, Sigma, Cat #: A9647) in 1x TBS with 0.1% Tween-20 (1x TBSTw). Pgk1 mouse monoclonal antibody (1:3000 dilution, Invitrogen, Cat #: 459250) and GFP Living Colors A.v. mAb clone JL-8 (1:1000 dilution, Takara Bio, Cat #: 632381). The membrane was washed 4x for 10 min with shaking in 1x TBSTw, and then incubated with fluorescent IRDye secondary antibodies for 1 hour with rotation (1:10,000 dilution, LI-COR, cat #: 926-32210 and 926-68071). The membranes were washed 2x for 5 minutes each with 1x TBSTw followed by 2 washes with 1x TBS (no Tween). Membranes were imaged on LI-COR Odyssey® Fc Imaging system and analyzed in Image Studio (LI-COR) software.

Drug treatments

β-estradiol (E2758-1G, Sigma-Aldrich) was dissolved in ethanol and 1 μM was added to SC medium after HS to induce expression of Hsp104. Guanidine hydrochloride (GdnHCl, 15502-016, Invitrogen) was dissolved in DMSO and 3 mM was used to inhibit Hsp104 and was added either at 0 or 30 min after HS where indicated. For GdnHCl washout experiments, cells were heat shocked and allowed to recover for 0 or 30 min, incubated with GdnHCl for 1 hour, washed 3x with fresh SC complete and then imaged over time.

QUANTIFICATION AND STATISTICAL ANALYSIS

Statistical analysis

Statistical analysis was performed via an unpaired two-tailed t-test or via a one-way ANOVA with a *p* value <0.05 followed by a Tukey post hoc test and (H) via an unpaired two-tailed t-test with the following significance cut-off: not significant (NS): *p* > 0.05, *: *p* ≤ 0.05, **: *p* ≤ 0.01, ***: *p* ≤ 0.001, ****: *p* ≤ 0.0001 with GraphPad Prism. The number of replicates and cells are indicated in the figure legends. No statistical methods were used to predetermine the sample size. The experiments were not randomized, and the investigators were not blinded to allocation during experiments and outcome assessment.